ADDIS ABABA UNIVERSITY

ADDIS ABABA INSTITUTE OF TECHNOLOGY

SCHOOL OF CIVIL AND ENVIRONMENTAL ENGINEERING

GEODESY AND GEOMATICS PROGRAM

PREDICTING FUTURE URBAN LAND SURFACE TEMPERATURE FROM SPATIO-TEMPORAL LAND USE LAND COVER DYNAMICS: A CASE OF ADDIS ABABA CITY AND SURROUNDINGS, ETHIOPIA.

BY WENDWESEN TADDESSE SAHILE

JANUARY 2021

ADDIS ABABA, ETHIOPIA

Addis Ababa University

Addis Ababa Institute of Technology

School of Civil and Environmental Engineering

A THESIS SUBMITTED TO

THE SCHOOL OF GRADUATE STUDIES OF ADDIS ABABA UNIVERSITY IN PARTIAL FULFILLMENT OF THE REQUIREMENTS FOR MASTER OF SCIENCE IN GEODESY AND GEOMATICS, SPECIALIZATION IN GEOMATICS

BY:

WENDWESEN TADDESSE SAHILE

GSR/2525/11

ADVISOR:

DR. BINYAM TESFAW (ASST. PROFESSOR)

JANUARY 2021

ADDIS ABABA, ETHIOPIA

DECLARATION

I, the undersigned, declare that the thesis titled "Predicting Future Urban Land Surface Temperature from Spatio-Temporal Land Use Land Cover Dynamics: A Case of Addis Ababa city and Surroundings, Ethiopia" carried out under the supervision of **Dr. Binyam Tesfaw** is my own work and has not been presented for a degree in any other university and that all sources of material used for the thesis have been appropriately acknowledged.

Wendwesen Taddesse	----------	----------
Name of Candidate	Signature	Date

As Master research advisor, I hereby certify that I have read and evaluated this MSc thesis prepared under my guidance.

Dr. Binyam Tesfaw	----------	----------
Name of Advisor	Signature	Date

Approval Sheet

Addis Ababa Institute of Technology

School of Civil and Environmental Engineering

The undersigned have examined the Thesis entitled "***Predicting Future Urban Land Surface Temperature from Spatio-Temporal Land Use Land Cover Dynamics: A Case of Addis Ababa city and Surroundings, Ethiopia***." Presented by **Wendwesen Taddesse Sahile,** a candidate for the Degree of Master of Science in Geodesy and Geomatics and herby certify it is worthy of acceptance.

Board of Examiners Committee:

Dr. Binyam Tesfaw ---------- ----------

Advisor Signature Date

Dr. Berhan Gessesse ---------- ----------

Internal Examiner Signature Date

Dr. Worku Zewdie ---------- ----------

External Examiner Signature Date

Dr. Ing. Mebruk Mohammed ---------- ----------

Chairperson Signature Date

ACKNOWLEDGMENT

First of all, I would like to thank the "**Almighty GOD**", who helped me to accomplish my thesis. A special thanks to my advisor, **Dr. Binyam Tesfaw** for being generous in sharing knowledge for this study; for the guidance, support, and encouragement throughout; for devotedly contributing towards the success of this study. Your words of inspiration and confidence in me will never be forgotten. I also want to thank those seniors who paved the way to my journey in my academic career. Last but not least I appreciate those people around me with the courage to date that has a profound positive impact on my academic journey.

Table of contents

LISTS OF FIGURES

LISTS OF TABLES

ACRONYMS

CA	Cellular Automata
CSA	Central Statistical Agency
DN	Digital Number
ERDAS	Earth Resources Data Analysis Systems
EROS	Earth Resources Observation System
ETM+	Enhanced Thematic Mapper plus
GIS	Geographical Information System
GPS	Global Positioning System
KIA	kappa index of agreement
LST	Land Surface Temperature
LCI	Land Cover Indices
LULC	Land Use Land Cover
MNDWI	Modified Normalized Difference Water Body Index
NDBI	Normalized Difference Built-Up Index
NDVI	Normalized Difference Vegetation Index
NDWI	Normalized Difference Water Body Index
OLI	Operational Land Imager
RS	Remote Sensing
SAVI	Soil Adjusted Vegetation Index
SPSS	Statistical Package for Social Science
SRTM	Shuttle Radar Topographic Mission
TIRS	Thermal Infrared Sensor
TM	Thematic Mapper
UI	Urban Index
USGS	United State Geological Survey

ABSTRACT

***A**lthough several studies were conducted on modeling future land use land cover (LULC) change in Ethiopia, predicting future urban land surface temperature (LST) from LULC dynamics is less common. **T**he objective of the study was to predict the future LST of Addis Ababa city and its surrounding area from LULC dynamics. **F**our Landsat (TM, ETM+, and OLI-TIRS) images were used to extract and map LST and LULC distribution for the years 1991, 2002, 2011, and 2020. The performances of several land cover indices (LCI) to predict LST were assessed. CA-Markov chain analysis was applied to predict the LULC and LCI of 2050. The regression analysis was applied to project the future LST from LCI. **T**he finding of the study indicated that the NDBI was the top selected for the prediction of the future LST with the highest correlation(R = 0.72). LST was predicted from NDBI with a mean absolute percentage error(MAPE) of 9.4%. The LULC changes between 1991 and 2020 showed that the built-up area was increased by 38000 ha whilst the water bodies, agriculture, and vegetation areas were decreased by 172 ha, 26905 ha, and 10920 ha, respectively from 1991 to 2020. Between 2020 and 2050, the coverage of the built-up area was predicted to increase by 26013 ha while the area coverage of water bodies, agricultural land, and vegetation area was predicted to decrease by 16 ha, 19133 ha, and 6864 ha, respectively. Between 1991 and 2020, the area coverage of the lowest LST range (10 –20 ^{0}C) was decreased by 14728 ha while the area covered by the highest LST range(34 – 45 ^{0}C) was increased by 16051 ha. The predicted LST result from NDBI showed that the lowest category was predicted to decrease by 544ha while the highest category was predicted to increase by 3353 ha from 2020 to 2050. **A**nd hence it was concluded that the rise of LST will continue in the future due to the LULC changes and global climate warming unless properly mitigated.*

Keywords: Addis Ababa City, Cellular Automata Markov, Land Cover Indices, Land Surface Temperature, Land Use Land Cover, Normalized Difference Built-up Index, and Regression analysis

CHAPTER 1 INTRODUCTION

1.1 Background

The surface of the earth has been continuously changed over time. This continuously changed surface introduces environmental change. Global Land Use Land Cover(LULC) dynamics have contributed to worldwide climate change(Ramachandra et al., 2012). The change in LULC leads to environmental problems like seasonal fluctuation and the rise of sea-level and land surface temperature (LST). Africa is the most susceptible continent to climate change and the rise of temperature, drought, and the variability of rainfall has been observed due to this climate change(Parry et al., 2007). The combined influence of variability and change of climate is higher in Ethiopia because most activities in the country are climate-sensitive. The rising of temperature as well as the variability of rainfall was observed in Ethiopia(NMA, 2007). The variability in rainfall and the rise of temperature in Ethiopia affected the water resources, health, and livestock(Gezie, 2019).

The LST has been affected by Atmospheric conditions and land cover types(Zhang et al., 2009b). Among these, the LST has been severely affected by LULC dynamics. The rapid population growth and a higher rate of urbanization introduced wide LULC changes. Urban expansion is a cause for the replacement of natural surfaces by artificial (heat-absorbing) surfaces. This affects the evapotranspiration characteristics of the land surface and makes the urban area have higher LST than the nearby areas(Rao, 1972, Lo et al., 2003, Gluch et al., 2006, Amiri et al., 2009, Hu and Jia, 2010). Directly or indirectly the growth of population minimizes the coverage of vegetation as this land is required for various activities. This decrement of the vegetation coverage introduced the rise in LST(Julien and Sobrino, 2009). Appropriate deployment of natural resources is essential as the size of Land is do not vary with population number(FAO, 1999).

Investigating and simulating the change of LULC is significant for various planning and controlling in urban land management(Regmi et al., 2017). Observation of the past and identifying the current LULC change helps to identify the trend of the dynamics and enable to forecast the future(Omar and Sanusi, 2014).

1.2 Statement of the Problem

Population growth and urban expansion have been introduced wide LULC changes and lead to seasonal instability and the rise of temperature. In Ethiopia, the temperature rise affected the availability of natural resources and community health(Gezie, 2019). These problems may continue unless properly mitigated by examining the historical change and estimating the future change in the temperature. The future distribution of temperature has been projected via regional and global models(Hoffmann et al., 2012). These global and regional models produce data with low resolution, which requires additional downscaling. Due to their availability in lower resolution, they are not appropriate for identifying the change in the surface temperature at a localized scale(Smith et al., 2011).

Studies have been examined the impact of LULC changes on urban LST in Addis Ababa city and identified that rapid urban expansion and the rise of LST(Tafesse, 2017, Balew, 2018, Abraha, 2012). However, they focused only on detecting the effect of historical LULC change on LST. Other studies were focused on simulating future LULC change in the study area using the combined Cellular Automata and Markov chain (CA-Markov) model(Mohamed and Worku, 2019). The result depicted that a constant increment of the built-up area at the expense of other LULC classes. But, the result didn't state the consequence of the predicted LULC change on the forthcoming change on LST in the study area.

Although several studies were conducted on modeling future LULC and others showed the impact of historical LULC change on LST as well, in Ethiopia predicting future urban LST from LULC dynamics is less common. The study was aimed at filling the existing gap by simulating future LULC changes of Addis Ababa city and surrounding area using the CA-Markov model and predicting future LST using regression analysis. The regression analysis helped to model the relationship between Land Cover Indices (LCI) and LST for the prediction of future LST.

CA-Markov can simulate and model future LULC change and can equally offer information on future changes on LST(Ahmed et al., 2013). Furthermore, the study provides the past, current, and future changes on LST and LULC in the study area. This helps to encourage viable urban development that redirects the upcoming distribution of LULC and LST, alleviation activities for the rise of LST. Finally, the finding of the study will provide information that helps to make the right decision at the right time.

1.3 Objectives of the Study

1.3.1 General Objective

- The main objective of the study was to predict the future LST of Addis Ababa city and its surrounding area for the year 2050 from Spatio-Temporal LULC dynamics.

1.3.2 Specific objectives

- To quantify the Spatio-Temporal changes of LULC and LST from 1991 to 2020 of the study area.
- To identify and select the variable that best predicts LST and predict the LST of the study area.
- To model future changes on LULC of the study area for the year 2050.

1.4 Research Questions

- What is the Spatio-temporal change of LST and LULC between 1991 and 2020 in Addis Ababa city and its surrounding area?
- What is the variable that best predicts the LST of the study area for the year 2050?
- What is the extent of LULC of the study area for 2050?

1.5 Significance of the Study

The study offers valuable information regarding the past and future changes on the LULC and LST in the study area. The findings of the study could be used by government policymakers, urban and rural land managers, natural resources managers, environmental experts, and other concerned bodies for their decision-making processes related to how LULC and LST change through time. Additionally, it could be used as a reference for further studies related to LULC and LST change over time.

1.6 Scope of the Study

The study assessed the Spatio-temporal dynamics of LULC and LST of Addis Ababa city and its surrounding area between 1991 and 2020. Additionally, the future urban LULC change was modeled using the CA-Markov model for the year 2050. Finally, the relationship between LCI and LST was examined for the prediction of future LST change for the year 2050. The regression model was applied to convert the modeled LCI to LST for the year 2050.

1.7 Limitation of the study

Gathering socioeconomic data related to the whole study area was difficult due to the selected study area boundary was not an administrative boundary. All the population and climate data describing the study area belong to Addis Ababa city, not the whole study area. To model LULC change for 2050 using the CA-Markov model precisely, it was better to use the 1990 satellite as the initial map and 2020 as the base map (30 years back and forward from 2020). But, the 1991 image was used instead of 1990 as the initial image in the CA-Markov model to minimize the cloud coverage.

1.8 Thesis Structure

The thesis was organized into six chapters.

Chapter one encompasses the background, statement of the problem, research questions, objectives, significance, scope, and limitations of the study. Chapter two consists of Literature review parts and included the idea behind LULC and the impact of LULC on LST, retrieval of LST, LCI, and modeling LULC. Chapter three consists of the description of the study area, data, and the software used, image classification, retrieval of LST, and selection of LCI for prediction of LST. Chapter four presents the results of the study including spatial distribution of LULC, LULC change detection, spatial distribution of LST, relationship between LCI and LST, prediction of LULC and LST, and the relationship of LST and precipitation with LULC. Chapter five describes the discussion of the result obtained in chapter four. Chapter six contains the conclusion and recommendation of the study.

CHAPTER 2 LITERATURE REVIEW

2.1 Concepts of Land Use Land Cover Change

The earth's surface has been altered extensively in the previous time by human-induced factors like agricultural activities, deforestation, and urbanization. The explanation of land use and land cover has been used as the same in many studies which are not. Land-cover denotes the physical cover of the land including vegetation, bare soil(Ellis and Pontius Jr, 2006). Land-use is the utilization of the land by human activities for settlements, agriculture, and forestry purpose(Di Gregorio, 2005). Land cover is a difference in the surface element that occurs when a surface has changed between two consecutive times(Lemlem, 2007). LULC change occurs initially at the parcel level when administrators decide to change from one land cover type to another land cover(Meyer and Turner, 1992).

In Ethiopia, the availability and managing of land resources vary due to the difference in climate and topography. The change in LULC alters the availability of vegetation and water(Ali, 2009). In the Ethiopian highlands, agricultural activities have played a fundamental role in the depletion of natural resources(Miheretu and Yimer, 2018). Some studies stated that forest coverage has been increased in the country during the period 1958–2006(Bantider et al., 2011). On the other hand, several studies reported that agricultural lands have been expanded at the expense of vegetation(Deribew and Dalacho, 2019, Zeleke and Hurni, 2001).

2.1.1 Drivers of land use land cover change

The main causes of LULC changes in Ethiopia are anthropogenic and naturally occurred processes(Agarwal, 2002). The natural and manmade factors influenced the change that occurred on LULC through time(Houghton, 1994). Population growth played a crucial role in many problems including the occurrence of the LULC change. Well-known drivers of LULC are the Natural process including climate change and direct and indirect influences of human activities(USEPA, 2004). The loss of soil and diminution of nutrients are implications of Land degradation(Tefera, 2002)

2.1.2 Impacts of Land Use Land Cover change on Land Surface Temperature

RS data are widely used to study the dynamics of current LULC and predict the future change of LULC. Studying the temporal and spatial dynamics of LULC has extensive significance in the study of LST. The environmental changes, growth of the human population, and economic development are key causes of LULC change(Houghton, 1994). The LULC dynamics become problems and major driving causes for the changes in the environment(FAO, 1999).

Currently, about half of the world's population exists in urban areas and expected to exist 68% in 2050(DESA, 2018). This trend in overall urbanization motivated various scholars to investigate the possible effects of urbanization on the environment such as the LST effect(Ye et al., 2010). Climate change is a combination of global warming caused by the releases of greenhouse gases and the extensive changes in weather forms(Qin et al., 2014).

Many studies showed the relationship between LULC and LST(Rahaman et al., 2018, Amiri et al., 2009, Xu et al., 2013, Jiang and Tian, 2010). Some of them studied the seasonal variations of temperature(Sung and Greening, 2013, Odindi et al., 2015) and identified the impact of different LULC classes on LST varies. Others showed the relationship between LULC and LST without predicting the temperature(Yuan and Bauer, 2007, Tran et al., 2006).

The LULC change effect on LST can be minimized by reducing the pavement materials and shading the roof with green plants(Adinna et al., 2009). Surfaces with high albedo and vegetation can affect the urban temperature(Akbari et al., 2001). Planting trees can reduce the rise of temperature and minimize air pollution in industrial areas(El-Nahry and Rashash, 2013). The LST in urban areas is higher than in vegetation areas since vegetation areas contribute to lower evaporation and transpiration. Different LULC categories can alter the LST conditions in cities. Understanding the interrelationship between LULC and LST can improve urban planning (Santana, 2007).

2.1.3 Land Use Land Cover Change Detection

LULC change detection is finding changes in the features covering the ground through time. Nowadays, it is used to manage the impact of natural processes on climate variability(Story and Congalton, 1986). Additionally, it can help to monitor the long term effect of LULC dynamics on human life and environmental change(Congalton, 2009). LULC change can be detected using different techniques by utilizing two classified maps of different years. Among these techniques post-classification comparison (PCC) is a method used to detect LULC change(Foody, 2002)

2.2 Land Surface Temperature Retrieval from RS Data

Among available approaches for measuring the thermal situations, RS-based measurement has an advantage by detecting spatially adjacent thermal characteristics over large areas at a time(Yue et al., 2007). Moreover, the RS method can provide measurements regarding the effects of LST on metropolitan areas(Yuan and Bauer, 2007). The Landsat sensors have sufficient resolutions for sensing the surface temperature(Yue et al., 2007).

2.2.1 Land surface emissivity

Land Surface emissivity (LSE) is a measure of the effectiveness of a material in emitting thermal radiation. It depends on moisture content, surface roughness, and observation condition(Sobrino et al., 2001). For natural land surface, the emissivity is affected by soil composition, vegetation appearances, and the content of moisture(Van de Griend and OWE, 1993). Understanding emissivity assists to lessen the error that arose on LST. Surface emissivity has a strong dependency on LULC and seasonality(Sobrino et al., 2001).

2.2.2 Land Surface Temperature

LST is the earth's surface temperature resulting from solar radiation that shows how hot the surface would feel to touch(Kayet et al., 2016). Air temperature and LST are not similar since air becomes cooler and hotter slowly than the land(Oyler, 2016). LST is essential for evaluating land-atmosphere interaction and limiting surface energy budgets(Sobrino et al., 2004). Due to the rise of LST, problems like the melting of ice and unexpected rainfall may occur(Weng and

Larson, 2005). The LST can be calculated from brightness temperature and surface emissivity(Rajeshwari et al., 2014).

2.3 Land Cover Indices

From Normalized Difference Vegetation Index (NDVI) values, the state of vegetation can be easily identified. Chlorophyll absorbs the visible light and reflects near-infrared light(Turvey and Mclaurin, 2012). NDVI is used to calculate LST from RS data(Omran, 2012) and calculated from reflectance in the red and the near-infrared portion. The lowest value of NDVI indicates pure water and the highest value shows green vegetation(BURGAN and Hartford, 1993). In areas where the surface of the soil is exposed due to less availability of vegetation, the vegetation index values can be influenced by the reflectance of the red and near-infrared spectrum(Huete, 1988). This problem is noticeable when the area has different soil types. The soil adjusted vegetation index(SAVI) was developed to correct this influence of soil brightness with lower vegetation cover(Huete, 1988). From SAVI values several vegetation characteristics like biomass properties and productivity can be identified(Colwell, 1974).

Normalized Difference Vegetation Index (NDBI) identifies the extent of impervious areas and highlights the built-up areas(Zha et al., 2003). Urban areas have more reflectance in the short-wave infrared(SWIR) band than the near-infrared (NIR) band(Alhawiti and Mitsova, 2016). The higher values of NDBI show areas of high density built-up while the lower values indicate non-built-up areas. Urban index (UI) is used to extract information regarding the urban sprawl from RS data(Kawamura, 1996).

2.4 Land Use Land Cover Modeling

Modeling involves the use of artificial representations of LULC changes and identification of future development. LULC change can be modeled based on the change in the past, current, and expectation of future change(Qiang and Lam, 2015). It plays a substantial role in the understanding of the changes that occur through time. Several simulation models have been developed to predict the change that occurred in LULC(Hu et al., 2007, Eastman et al., 2005).

IDRISI Selva software comprises environmental monitoring and modeling tools. Commonly used tools in IDRISI are GEOMOD, Land Change Modeler (LCM), Markov Chain, Cellular

Automata (CA), and CA-Marko(Eastman, 2006). The capability of the models varies with the output required. GEOMOD identifies the change between two LULC classes for the prediction of future LULC change while CA-Markov uses more LULC classes to simulate future change(Pontius and Malanson, 2005).

2.4.1 GEOMOD

It is widely used to examines the conditions of deforestation(Pontius Jr and Chen, 2006). It simulates future LULC changes from the past and the current LULC change. Both images should have the same number of LULC classes for input to provide suitability maps. Using change between only two classes as input is its limitation(Pontius Jr and Chen, 2006).

2.4.2 Land Change Modeler (LCM)

LCM concerned with the problem of hastened land change and for systematic requirements of biodiversity preservation(Eastman, 2012b). It is significant for ecological monitoring and a study of the change in LULC. It helps to decide on urban management(Fan and Shibata, 2015). The model can predict the change occurred by using additional suitability maps to the initial and later LULC images. Due to this, other models are selected rather than LCM(Adhikari and Southworth, 2012).

2.4.3 Markov chain model

It examines the probability of state one (t1) is changed to state two (t2). The future change is completed from two LULC images of two different periods(Moghadam and Helbich, 2013). The transition probability matrix shows the probability to change from one state to every other state. The transition area matrix stores the probable number of pixels changed over time(BEHERA et al., 2012). Markov chain model is not good at showing the spatial distribution of features(Schiff, 2011).

2.4.4 Cellular Automata (CA)

Cellular automata (CA) is cellular spaces, tessellation, and homogeneous structures(Wolfram, 1983). The CA model comprises a regular grid of cells and by apprises, the rule of the state of each cell is similar and is functional to the entire grid simultaneously(Schiff, 2011). CA shows

the spatial distribution of predicted LULC changes from transition matrices and suitability maps which are the outputs of Markov chain models. CA model is good at showing the spatial distribution of land features that obtained from Markov chain model.

2.4.5 Cellular-Automata Markov model

The Markov model predicts LULC change quantitatively without showing the LULC change. CA can forecast the transition between available categories(Gil, 2005). CA-Markov model can execute LULC the change in both time and dimensions by linking Cellular Automata and Markov. By using the quantity of change which is calculated through the Markov chain analysis; the CA-Markov model produces a LULC map at a later time. It transforms the output of the Markov chain to a spatially explicit model. CA-Markov Predicts the future distribution of LULC from multi-temporal LULC maps and Suitability maps. It can easily understandable but not consider Socioeconomic factors(Adhikari and Southworth, 2012).

These models are efficient for simulation by integrating the Markov-chain model with cellular automata(Keshtkar et al., 2016). These spatial models are widely applied for the analysis of LULC changes in time(Weng, 2002). Generally, the Markov Chain model's outputs are used as an input in CA models during prediction.

CHAPTER 3 MATERIALS AND METHODOLOGY

3.1 Description of the Study area

3.1.1 Location

Addis Ababa is the capital city of Ethiopia and is where the African Union is headquartered. Due to its historical, political, and diplomatic significance, the city is called the political capital of Africa. The geographical location of the study area is 08^0 47′ – 09^0 08′ N and 38^0 36′ – 38^0 56′ E. From the total area of the study area (1323.69km^2), Addis Ababa city covers 40.80% (540km^2) and the surrounding areas cover 59.20% (783.69km^2) which are parts of the Oromia region.

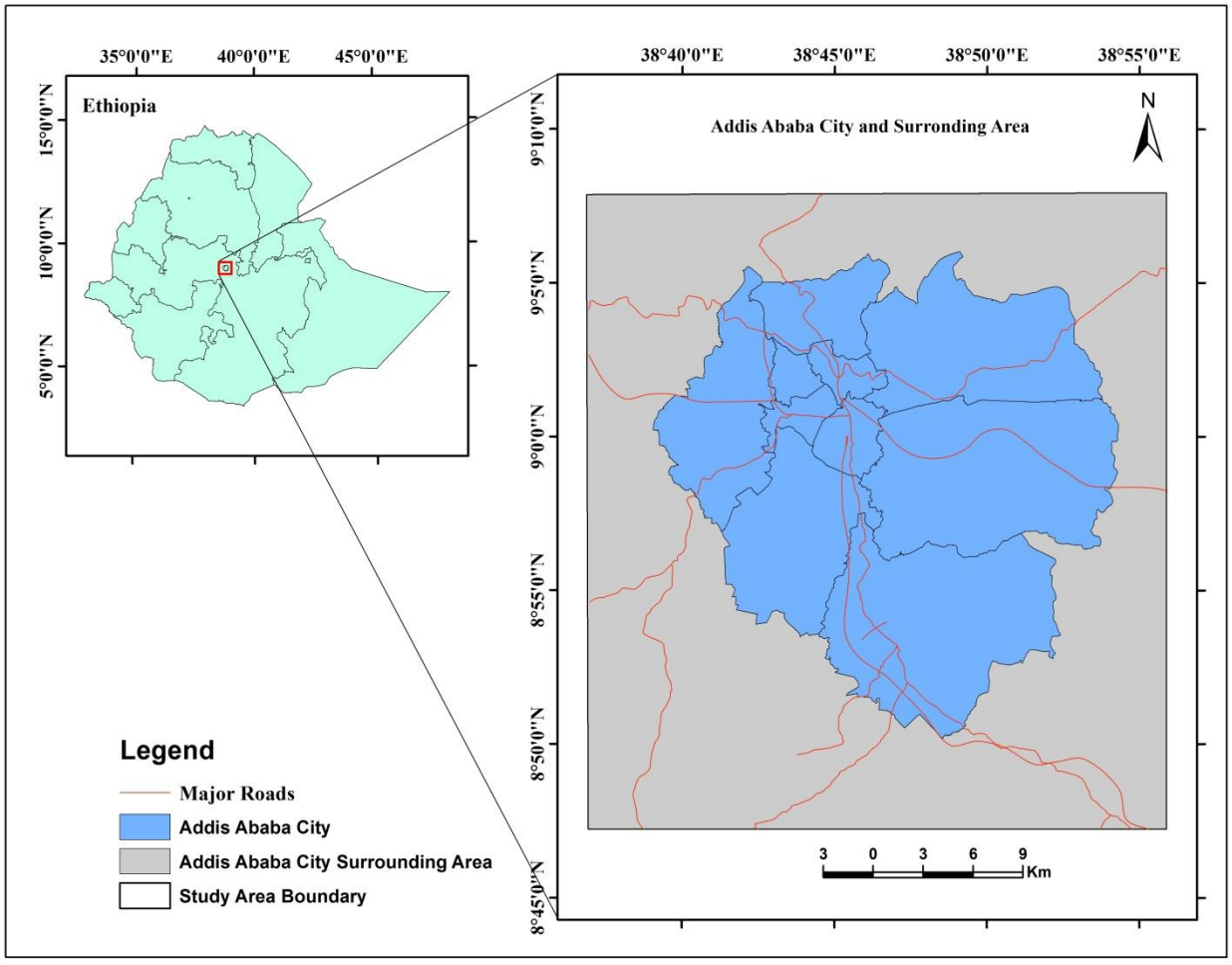

Figure 3.1 Study Area Map

3.1.2 Topography

The elevation of the study area ranges from 1895m to 3190m above mean sea level. The southern part of the study area, including the Akaki Kality area, has a lower elevation whilst the northern part of the study area including mount Entoto has a higher elevation. The central part has a medium elevation when compared to the other parts. Figure 3.2 shows the elevation map of the study area extracted from SRTM 30m (downloaded from the USGS Earth Explorer website).

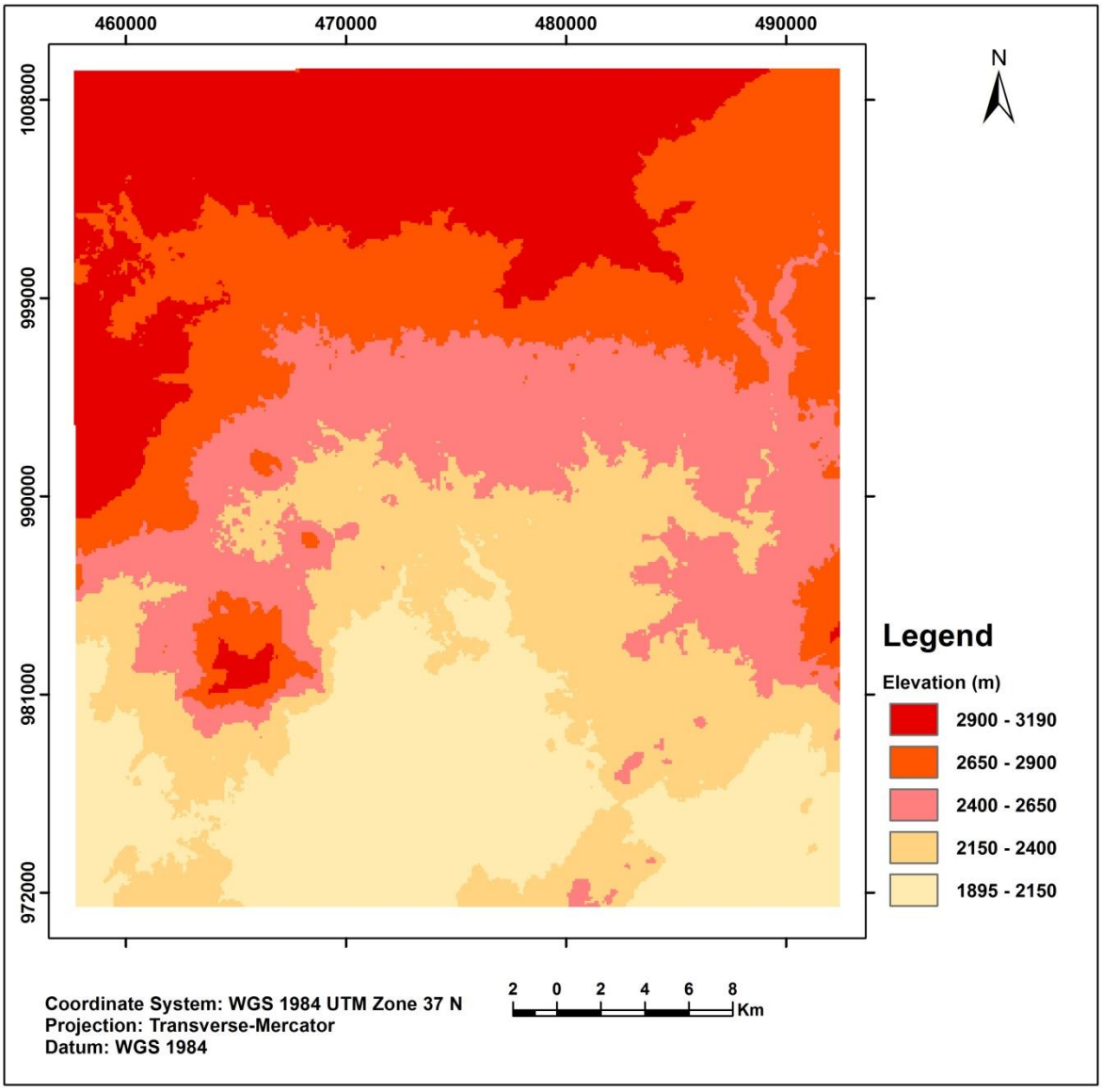

Figure 3.2: Study area elevation map

3.1.3 Population

The population of Addis Ababa city in 2007 was two million seven hundred thirty-nine thousand five hundred fifty-one (2,739,551). After eight years, the population number increased by 81.73% and reached three million three hundred fifty-two thousand (3,352,000) in the year 2015(CSA, 2015).

3.1.4 Climate

Addis Ababa city has a subtropical climate that varies with the month(Kottek et al., 2006). The average monthly temperature varies between 10 °C and 20 °C. The maximum temperature recorded was 25.2 °C in May and the minimum temperature recorded was 7 °C in December. The city has a rainfall peak between July and August and minimum rainfall between December and February. Figures 3.3 and 3.4 show the mean monthly temperature and an average rainfall of Addis Ababa city between 2009 and 2019, respectively[1].

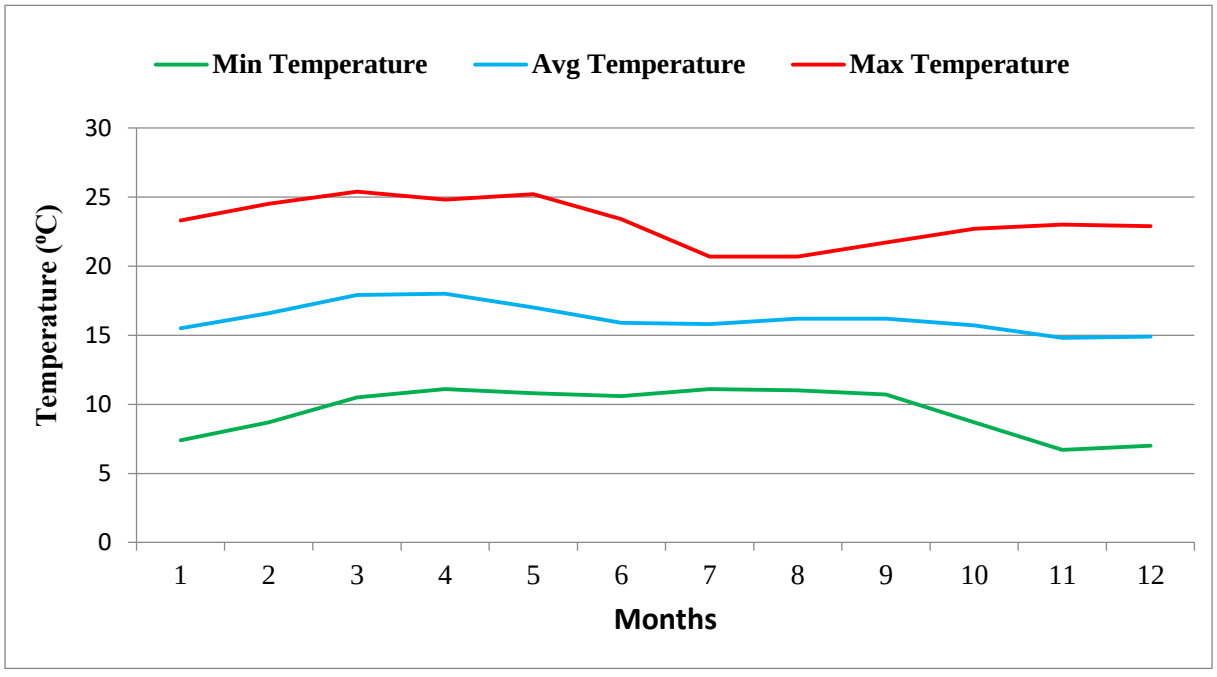

Figure 3.3: Mean monthly temperature of Addis Ababa city between 2009 and 2019

[1] www.worldweatheronline.com/addis-ababa-weather

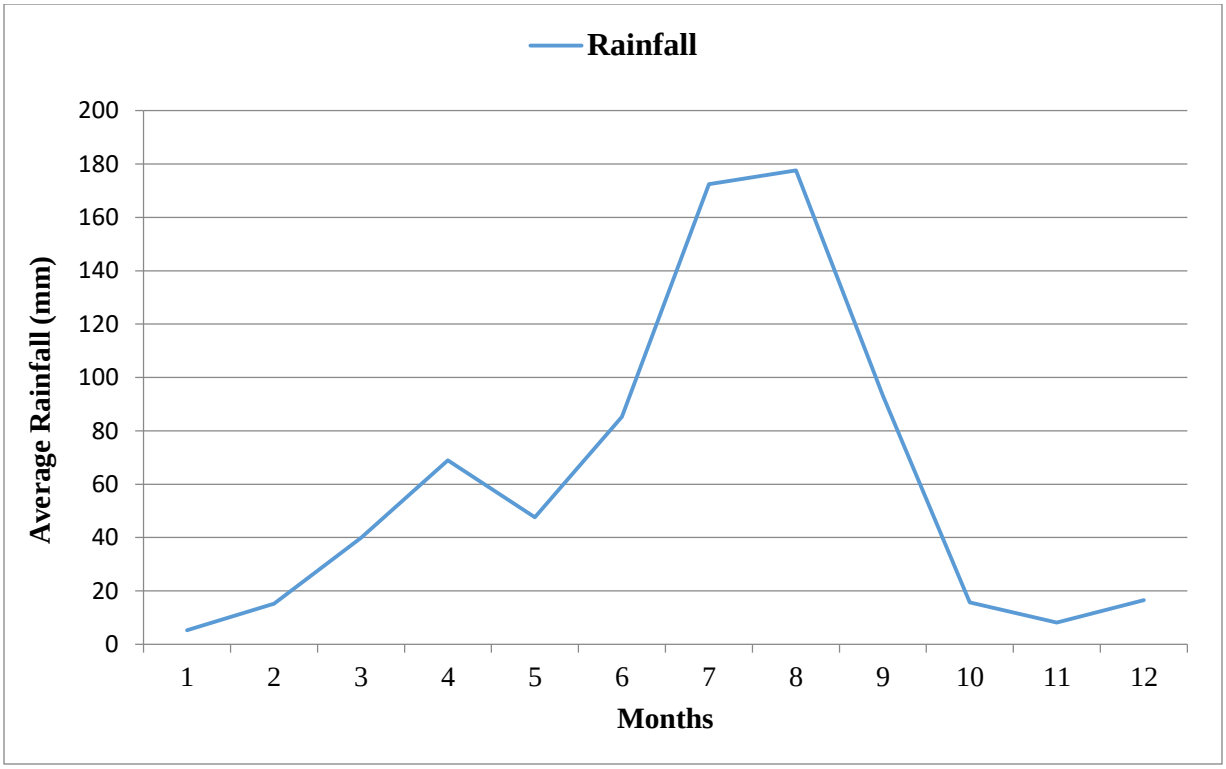

Figure 3.4: Mean total rainfall of Addis Ababa city between 2009 and 2019

3.2 Data and Data source

Four Landsat data (TM of 1991 and 2011, ETM+ of 2002, and OLI-TIRS of 2020) with a Path 168 and Row 54 were downloaded from the United States Geological Survey (USGS) Earth Explorer websites for classification of LULC and retrieval of LST. All these images were acquired in January to minimize cloud coverage (<0.03). Landsat 7 ETM+ of 1991 of the January has higher cloud cover. Due to this, the Landsat 5 TM was used instead. Again for the year 2011, Landsat 7 has a striping problem. Similarly, Landsat 5 TM was used for the year 2011. Ground reference points were collected using Handheld GPS for assessing the accuracy of the classification. Table 3.1 shows the data and data sources used.

Table 3.1: Data and data sources

Data Name	Acquisition Date	Spatial Res (m)	Cloud cover	Source	Path/ row	Purpose
TM	19/01/1991	30	0.00	USGS Earth Explorer	168/54	For LST retrieval and Image classification
ETM+	25/01/2002	30	0.00	"	"	"
TM	10/01/2011	30	0.00	"	"	"
OLI_TIRS	19/01/2020	30	0.02	"	"	"
Ground Truth data	-	-	-	Fieldwork and Google Earth	-	For accuracy assessment
SRTM	-	30	-	USGS Earth Explorer	-	To identify study area topography
Addis Ababa City Boundary	-	-	-	Addis Ababa City municipality	-	To extract/clip data to the study area

3.3 Software Packages and Instruments

3.3.1 Software Packages and Instruments

Table 3.2: Software packages and Instruments used

Software packages	Purposes
ArcGIS 10.5	Data analysis and map preparation
ERDAS IMAGINE 2014	For LULC classification and LST retrieval
Google Earth Pro	For reference in accuracy assessment
IDRISI Selva 17.0	For change analysis and modeling future LULC and LCI.
Quantum GIS 3.10	For downloading and processing Landsat Data
SPSS 16.0	For correlation and regression analysis for the selection of LCI in predicting LST
Handheld GPS	To collect ground truth data for accuracy assessment.

3.4 Methods

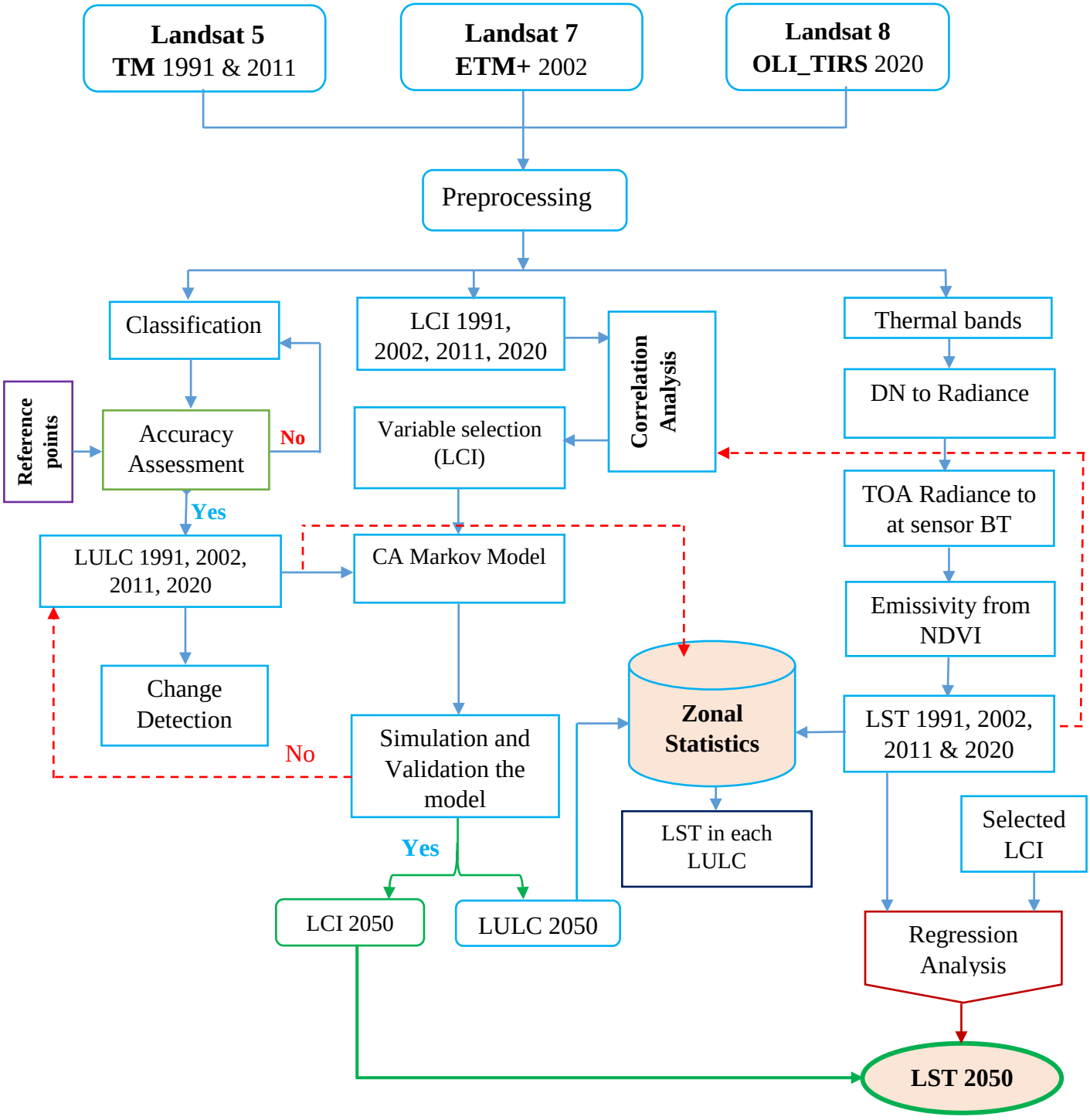

Figure 3.5: Methodology flow chart

3.5 Image Pre-Processing

Many image processing techniques assisted the investigation of RS data. Pre-processing the image increases the readability before classification. The selection of enhancement methods depends on the output required.

3.5.1 Atmospheric Correction

The measured radiance from the earth's surface is subjected to clouds and other particles in the atmosphere. Atmospheric correction was applied to remove the noises in the atmosphere by applying Dark Object Subtraction (DOS1) method under the preprocessing tool in Quantum GIS 3.10.

3.5.2 Geometric Correction

The USGS provides free geometrically corrected Landsat data collections which consist of a global set of TM, ETM+, and OLI_TIRS imagery.

3.5.3 Radiometric Calibration

Radiometric calibration is the conversion of DN to radiance and then to reflectance(Chander et al., 2009). For TM and ETM+ imageries, the DN values were first converted to the Radiance value. Then the radiance values of non-thermal bands were converted to reflectance. For OLI_TIRS, the DN values were converted to the spectral Radiance and again converted to top of atmospheric reflectance. The following steps were applied during radiometric calibration.

*3.5.3.1 **DN values conversion to Radiance***

Table 3.3 and 3.4 contain the TM and ETM+ calibration constants used for the radiometric calibration(Chander et al., 2009)

Table 3.3: TM calibration constants

Band No	Range	Centerλ	LMINλ	LMAXλ	Grescale	Brescale	ESUNλ
1	0.452 – 0.518	0.485	-1.52	169	0.671339	-2.19	1983
2	0.528 – 0.609	0.569	-2.84	333	1.322205	-4.16	1796
3	0.626 – 0.693	0.660	-1.17	264	1.043976	-2.21	1536
4	0.776 – 0.904	0.840	-1.51	221	0.876024	-2.39	1031
5	1.567 – 1.784	1.676	-0.37	30.2	0.120354	-0.49	220
6	10.45 – 12.42	11.435	1.2378	15.3032	0.055376	1.18	N/A
7	2.097 – 2.349	2.223	-0.15	16.5	0.065551	-0.22	83.44

Table 3.4: ETM+ calibration constants

Band No	Range	Center λ	LMINλ	LMAXλ	Grescale	Brescale	ESUNλ
1	0.452 – 0.514	0.483	-6.2	191.600	0.778740	-6.98	1970
2	0.519 – 0.601	0.560	-6.4	196.500	0.798819	-7.20	1842
3	0.631 – 0.692	0.662	-5.0	152.9	0.621654	-5.62	1547
4	0.772 – 0.898	0.835	-5.1	241.100	0.639764	-5.74	1044
5	1.547 – 1.748	1.648	-1.0	31.060	0.126220	-1.13	225.7
6	10.31 – 12.36	11.335	3.20	12.65	0.037205	3.16	-
7	2.065 – 2.346	2.206	-0.35	10.80	0.043898	-0.39	82.06
Pan	0.515 – 0.896	0.076	-4.7	158.3	0.641732	-5.34	1369

For TM and ETM+, the spectral radiance is calculated by the equation(Markham and Barker, 1986):

$$\mathrm{L}\lambda = \left(\frac{\mathrm{LMAX}\lambda - \mathrm{LMIN}\lambda}{\mathrm{QCALMAX} - \mathrm{QCALMIN}}\right) * (\mathrm{QCAL} - \mathrm{QCALMIN}) + \mathrm{LMIN}\lambda \ldots\ldots\ldots\ldots\ldots\ldots\ldots.\ldots\ldots\ldots.. (1)$$

Where:

Lλ - Spectral Radiance

QCAL - the quantized calibrated pixel value in DN

LMINλ – a radiance scaled to QCALMIN)

LMAXλ - a radiance scaled to QCALMAX)

QCALMIN = 1

QCALMAX = 255, from metadata file

For OLI-TIRS, DN values were converted to Radiance by the following equation using rescaling factors provided in the metadata file(USGS, 2016).

$$L\lambda = M\rho * Q\mathrm{cal} + \mathrm{AL} \ldots\ldots\ldots\ldots\ldots\ldots\ldots\ldots\ldots\ldots\ldots\ldots\ldots\ldots\ldots\ldots\ldots\ldots\ldots\ldots\ldots\ldots\ldots\ldots\ldots\ldots\ldots\ldots\ldots\ldots\ldots\ldots (2)$$

Where,

Lλ = TOA Reflectance,

AL = Reflectance additive scaling factor for the band

QCAL = L1 pixel value in DN

MP = Reflectance multiplicative scaling factor for the band

3.5.3.2 ***Radiance conversion to Reflectance***

The radiance values obtained in non-thermal bands of TM and ETM+ were converted to reflectance by the equation(USGS, 2016):

$$\rho\lambda = \frac{\pi . L\lambda . d^2}{ESUN\lambda \,\mathrm{Cos}\, \theta \mathrm{s}} \ldots\ldots\ldots\ldots\ldots\ldots\ldots\ldots\ldots\ldots\ldots\ldots\ldots\ldots\ldots\ldots\ldots\ldots\ldots\ldots\ldots\ldots\ldots\ldots\ldots\ldots\ldots\ldots\ldots\ldots\ldots (3)$$

Where,

Pλ - unit less planetary reflectance

Lλ - spectral radiance

d - the earth-sun distance

θs- Solar zenith angle (90-sun elevation angle)*(180/ π)

ESUNλ - is solar spectral irradiance, from(Chander et al., 2009)

The DN values in OLI were converted to Top of Atmospheric reflectance by the equation(USGS, 2016):

$$\rho\lambda' = M\rho * Qcal + A\rho \dots \dots \dots \dots \dots \dots \dots \dots \dots \dots \dots \dots \dots \dots \dots \dots \dots \dots \dots \dots \dots \dots \dots \dots \dots \dots \dots \dots \dots (4)$$

Where,

ρλ' = Spectral Reflectance, need additional correction for a solar angle.

Mρ = Reflectance multiplicative scaling factor

Aρ = Reflectance additive scaling facto

Qcal = pixel value in DN

But, ρλ' - requires a correction for the solar elevation angle and calculated by the equation(USGS, 2016):

$$P\lambda = \frac{\rho\lambda'}{\sin\theta SE} \dots \dots \dots \dots \dots \dots \dots \dots \dots \dots \dots \dots \dots \dots \dots \dots \dots \dots \dots \dots \dots \dots \dots \dots \dots \dots \dots \dots (5)$$

ρλ = TOA planetary reflectance

θSE = Local sun elevation angle; the scene center sun elevation angle in degrees is provided in the metadata.

3.6 Image Classification

Image classification is widely used in several RS applications for extracting thematic information. It combines pixels into more representative represent similar land features(Jensen, 1996). Classification requires an explicitly formulated algorithm for various purposes as it is highly dependent on the objective required.

Unsupervised classification: pixels with collective characteristics are clustered without the aid of the analyst. Once the number of classes is specified by the user, the software fixes which pixels are associated with and assembled them into classes. The analyst specifies the algorism used in the software and the variation within each category(Benayas et al., 2007).

Supervised classification: the analyst collects training samples from each category and orders the software to classify the remaining pixels accordingly(Perumal and Bhaskaran, 2010). Once

the training samples were collected, the image was classified using the maximum likelihood algorithm. The classification schemes used in the study were adopted from the AFRICOVER urban land classification scheme which is broadly practiced in East African Countries(FAO, 2002).

Table 3.5: classification of LULC in the study area

No	Class Name	Description
1	Agriculture	Rain feed arable lands, cultivated field, irrigated cropland and farming lands
2	Vegetation	Manmade and natural forests, shrubs, woodland, sparsely planted trees, and evergreen plants
3	Built-up	Land covered by buildings and other man-made structures such as residential, commercial, industrial area, railways, and road networks
4	Water bodies	Lakes, ponds, marshes, and rivers

Source:(FAO, 2002)

3.6.1 Accuracy Assessment

Accuracy assessment was used to validate the classification by assessing how pixels were assigned to the correct LULC classes. Google Earth's historical satellite image and ground truth data collected from the field were used to assess the accuracy of classification. At least 50 points per LULC class must be collected for areas less than 4000 km^2 and having fewer than 12 classes(Zhang et al., 2009a, MacLean and Congalton, 2012). Since the study area is known, the overall study was clustered into four LULC classes. Then the stratified sampling technique was applied to collect samples for assessing the accuracy. This has the advantage of representing each LULC class. The size of the study area is less than 4000 km^2 and there were four LULC classes. Thus, a total of 300 samples were collected from both Google Earth historical image and ground survey for 2020, and 400 samples were collected from Google Earth Historical image for 1991, 2002, and 2011. Figure 3.5 shows the sample points with satellite images for 1991 and 2020.

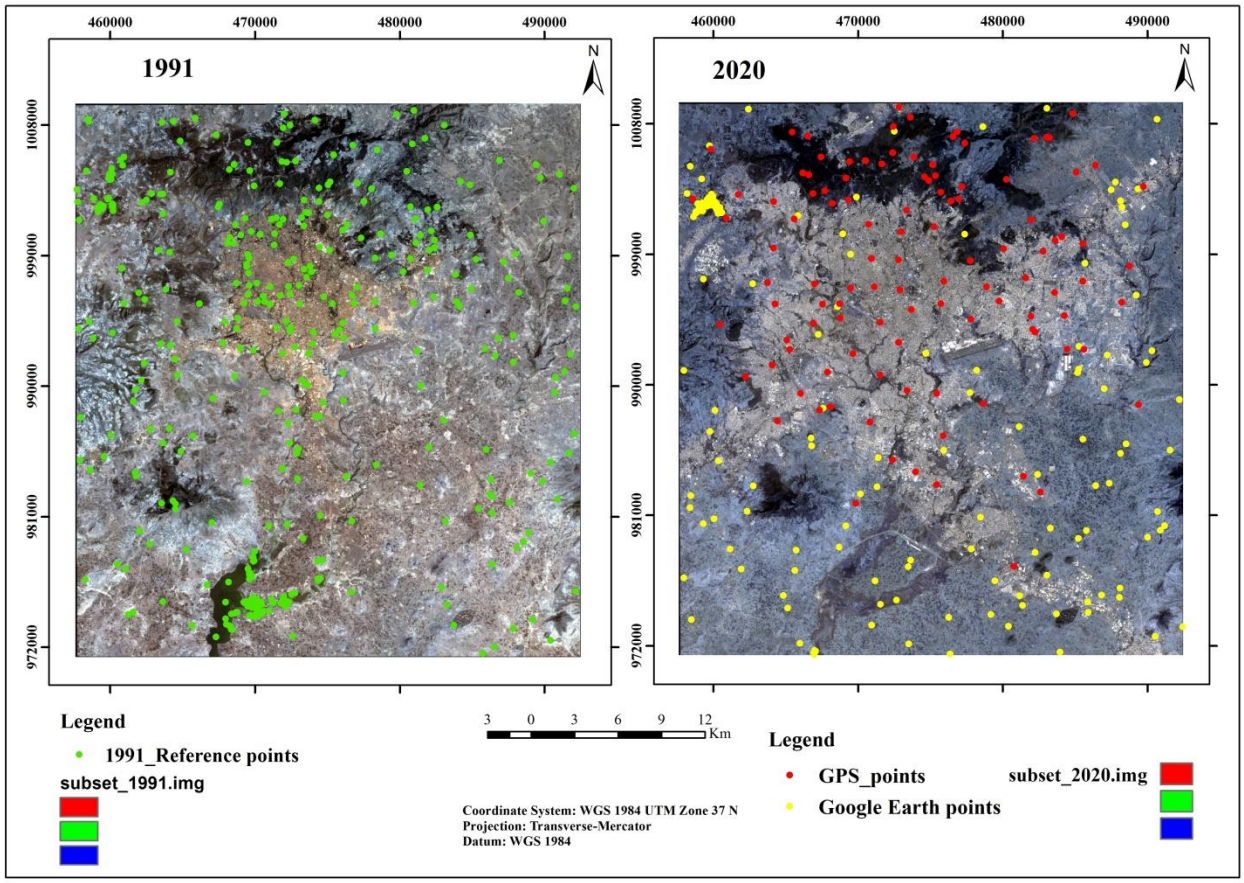

Figure 3.6: Sample reference points with satellite images for 1991 and 2020

The overall accuracy identifies the percentage of correctly classified pixels from the total pixels. But it misses how errors are distributed across each LULC category. To show this, the producer's accuracy and user's accuracy were applied. User's accuracy is the ratio of correctly classified pixels to classified total whereas the Producer's accuracy is the ratio of correctly classified pixels to Reference total pixels.

Table 3.6: Category of Kappa Statistics

Kappa statistics	< 0.00	0.00 – 0.20	0.21 – 0.40	0.41 – 0.60	0.61 – 0.80	0.81 – 1.00
Strength of agreement	Poor	Slight	Fair	Moderate	Substantial	Almost Perfect

Source: (Koch et al., 1977).

3.7 Land Use Land Cover Change Detection

The LULC changes were detected between two pairs of LULC maps between 1991 and 2020. The detections were held between the years (1991 – 2002, 2002 – 2011, and 2011 – 2020). Using post-classification comparison techniques the area of each LULC class changed to all other LULC classes were identified. The area coverage of the change in each LULC category can be identified in a change detection matrix. This matrix is a square matrix containing all LULC categories in rows and columns. Additionally, the rate of change of each LULC classes was calculated by the formula(Li, 2012)

$$R(\%) = \frac{(A2 - A1)}{(t2 - t1)(A1)} * 100 \quad \ldots\ldots (6)$$

Where,

R – Rate of change

A1 - Area of each LULC classes for the initial image

A2 - Area of each LULC classes for the later image

t1- specific year corresponds to the initial time

t2- specific year corresponds to the later image

The values of the rate of changes can be negative or positive to show either the LULC class has decreased or increased between the two years. The LULC categories decreased between two different years showed a negative rate of change values.

3.8 Computation of Land Cover Indices

Four LCIs (NDVI, NDBI, SAVI, and UI) were computed to examine their relationship with LST. Among these LCIs, NDVI and SAVI are used to identify the vegetation characteristics(Baloloy et al., 2018). Since the characteristics of the soil and the coverage of vegetation varies in the study area, SAVI was used as one variable to check if it has a strong correlation with LST. Even if UI and NDBI are used to identify the urban features from RS data, having extra indices increases the choice of variables that best predicts LST. Correlation analysis was applied between LCI and LST using SPSS 16.0 to select the index that best predicts LST.

3.8.1 Normalized Difference Vegetation Index (NDVI)

NDVI is commonly used to extract facts on crop production and coverage of green vegetation (Xiong et al., 2012). It is used as one variable to compute LST from RS data(Omran, 2012). The RED and NIR portion of the spectrum is used for the derivation of NDVI. The lower values of NDVI indicate an area covered by a water body whereas the higher values identify an area covered by green vegetation(BURGAN and Hartford, 1993). NDVI was computed by the formula(Tucker, 1979):

$$NDVI = \frac{NIR - RED}{NIR + RED} \dots \dots \dots \dots \dots \dots \dots \dots \dots \dots \dots \dots \dots \dots \dots \dots \dots \dots \dots \dots \dots \dots \dots \dots \dots \dots \dots \dots \dots \dots \dots \dots \quad (7)$$

Where:

NIR-Near-Infrared Band

RED- Red Band

3.8.2 Normalized Difference Built-up Index

NDBI can be Calculated from the Short-wave Infrared Band (SWIR (1.55 - 1.75 µm) for TM and ETM+ and (1.57 - 1.65 µm) for OLI_TIRS) and near-infrared band (NIR (0.76 – 0.9 µm) for TM and ETM+ and (0.85 - 0.88 µm) for OLI_TIRS). The higher values of NDBI indicate an area covered by built-up and the lower values indicate a non-built-up area. NDBI was calculated by the formula(Zha et al., 2003):

$$NDBI = \frac{SWIR - NIR}{SWIR + NIR} \dots \dots \dots \dots \dots \dots \dots \dots \dots \dots \dots \dots \dots \dots \dots \dots \dots \dots \dots \dots \dots \dots \dots \dots \dots \dots \dots \dots \dots \dots \quad (8)$$

Where:

SWIR-Short Wave Infrared band and

NIR-Near-Infrared Band

3.8.3 Urban Index

UI is used to produce information regarding urban sprawl from RS data(Kawamura, 1996). It was calculated from the Short-wave Infrared Band (SWIR2 (2.09 – 2.35 µm) for TM and ETM+ and (2.11 – 2.29 µm) for OLI_TIRS) and near infra-red (NIR (0.76 – 0.9 µm) for TM and ETM+ and (0.85 – 0.88 µm) for OLI_TIRS). UI was calculated by the formula(Kawamura, 1996):

$$UI = \left(\frac{SWIR2 - NIR}{SWIR2 + NIR}\right) \ldots\ldots\ldots (9)$$

Where:

SWIR – Short Wavelength Infrared band and

NIR – Near-Infrared band

3.8.4 Soil Adjusted Vegetation Index

The SAVI was developed to correct for the influence of soil brightness(Huete, 1988). Additional to NDVI, it was computed to predict LST because the soil characteristics and the coverage of vegetation across the study area vary. SAVI was calculated by the formula(Huete, 1988):

$$\text{SAVI} = \left(\frac{\text{NIR} - \text{RED}}{\text{NIR} + \text{RED} + \text{L}}\right) * (1 + \text{L}) \ldots\ldots\ldots (10)$$

Where:

SAVI – Soil adjusted vegetation index,

NIR – near-infrared,

L – Adjustment factor, L = 0.5 is common in most environmental conditions(Huete, 1988).

3.9 Land Surface Temperature Retrieval

LST was extracted from the thermal bands of Landsat images acquired in 1991, 2002, 2011, and 2020. It was computed from the two thermal bands (band 10 and band 11) in the Landsat 8 using a split-window algorithm. The use of simultaneously two bands and less sensitivity to uncertainties in the atmosphere makes the use of the split-window algorithm advantageous(Rajeshwari and Mani, 2014). But band 6 was used to compute the LST from Landsat 5 (TM) and Landsat 7 (ETM+). From the computed radiance values in section 3.4.3, the LST computation continued in this section.

3.9.1 Conversion of TOA Radiance to at Sensor Brightness Temperature (TB)

Table 3.7: TM, ETM+, and TIRS thermal bands calibration constants (from metadata file)

Sensor Name	Band Name	K1	K2
Landsat 5 TM	Band 6	607.76	1260.56
Landsat 7 ETM+	Band 6	666.09	1278.71
Landsat 8 TIRS	Band 10	777.8853	1321.0789
Landsat 8 TIRS	Band 11	480.8883	1201.1442

Brightness temperature was calculated from the spectral radiance of thermal bands by the formula(Weng et al., 2004, Rajeshwari and Mani, 2014):

$$TB = \frac{K2}{Ln\left(\frac{K1}{L\lambda} + 1\right)} \ldots \ldots (11)$$

Where:

TB - brightness temperature (K)

Lλ - TOA spectral radiance,

K1 - calibration constant 1, and

K2 - calibration constant 2, (Table 3.7)

3.9.2 Determination of Land Surface Emissivity

Emissivity is controlled by many factors including atmospheric water content and roughness of the surface. Emissivity has a strong association with NDVI and is computed from it by the formula(Weng and Larson, 2005, Rajeshwari and Mani, 2014):

$$\varepsilon = 0.004 * \mathrm{P}v + 0.986 \ldots \ldots (12)$$

Where:

ε – Land surface emissivity

Pv - Proportion of vegetation, and was calculated by the formula(Sobrino et al., 2004):

$$\mathrm{P}v = \left(\frac{\mathrm{NDVI} - \mathrm{NDVImin}}{\mathrm{NDVImax} - \mathrm{NDVImin}}\right)^2 \ldots \ldots (13)$$

Finally, LST was computed from the emissivity using(Xiong et al., 2012):

$$LST = \left(\frac{TB}{(1 + (\lambda * \rho) * \ln \varepsilon)}\right) \ldots \ldots \ldots \ldots \ldots \ldots \ldots \ldots \ldots \ldots \ldots \ldots \ldots \ldots \ldots \ldots \ldots \ldots \ldots \ldots \ldots \ldots \ldots \ldots \ldots \ldots (14)$$

Where:

LST – Land Surface Temperature

TB - Brightness Temperature in Kelvin,

λ - Wavelength of the emitted radiance (11.457 for TM and 11.269 for ETM+)

ε - land surface emissivity

$\rho = 1.438^{-2}$mK,

- **For the split-window algorithm, ε** was calculated by(Rajeshwari and Mani, 2014):

$$\varepsilon = \varepsilon s * (1 - FVC) + \varepsilon v * FVC \ldots \ldots \ldots \ldots \ldots \ldots \ldots \ldots \ldots \ldots \ldots \ldots \ldots \ldots \ldots \ldots \ldots \ldots \ldots \ldots \ldots \ldots \ldots (15)$$

Where,

ε - Land surface emissivity

εs - Emissivity for soil,

εv - Emissivity for vegetation (Table 3.8)

FVC - Fractional Vegetation Cover and calculated by(Rajeshwari and Mani, 2014):

$$FVC = \left(\frac{NDVI - NDVIs}{NDVIv - NDVIs}\right) \ldots \ldots \ldots \ldots \ldots \ldots \ldots \ldots \ldots \ldots \ldots \ldots \ldots \ldots \ldots \ldots \ldots \ldots \ldots \ldots \ldots \ldots \ldots \ldots \ldots \ldots \ldots (16)$$

Where: NDVI - Normalized Difference Vegetation Index,

$NDVI_V$ - shows NDVI for vegetation, and

$NDVI_S$ - shows NDVI for the soil & computed from NDVI(Jiménez-Muñoz et al., 2009)

Table 3.8. Emissivity values soil and vegetation

Emissivity	Band 10	Band 11
Es	0.971	0.977
Ev	0.987	0.989

Source: (Sobrino et al., 2004)

Table 3.9: Split Window Algorithm constant values

Constants	C_0	C_1	C_2	C_3	C_4	C_5	C_6
Values	0.268	1.378	0.183	54.300	-2.238	-129.200	16.400

Source: (Rajeshwari and Mani, 2014)

- **Using a split-window algorithm, LST was calculated by**(Jiménez-Muñoz et al., 2009)**:**

$LST = TB_{10} + C1(TB_{10} - TB_{11}) + C2(TB_{10} - TB_{11})^2 + C0 + (C3 + C4W)(1 - m\varepsilon) + C5 + C6W)\Delta\varepsilon$ ..... (17)

Where,

TB_{10} and TB_{11} – Brightness Temperature of Band 10 and 11

C_0, C_1, C_2, C_3, C_4, C_5, and C_6 – Split Window coefficient values from Table 3.9

$m\varepsilon$ – LSE Mean,

$\Delta\ \varepsilon$ – LSE difference, and

W – Atmospheric water vapor content

Primarily, LSE for band 10 and band 11 was computed. Then, the mean and the difference of LSE were computed from the calculated LSE of both bands. Finally, LST was calculated by equation (17). The Mean and the Difference of LSE of bands 10 and 11 were calculated as follows(Jiménez-Muñoz et al., 2009).

$$\text{LSEmean} = m\varepsilon = \frac{\text{LSEb10}+\text{LSEb11}}{2} \quad \text{and} \quad \text{LSEdifference} = \Delta\,\varepsilon = \text{LSEb10} - \text{LSEb11}$$

- **Conversion LST from the kelvin to degree Celsius unit**

$$\text{LST(celsius)} = \text{LST(Kelvin)} - 273.15 \ldots\ldots\ldots\ldots\ldots\ldots\ldots\ldots\ldots\ldots\ldots\ldots\ldots\ldots\ldots\ldots\ldots\ldots\ldots\ldots\ldots\ldots (18)$$

3.10 Selection of LCI for the Prediction of LST

The strength of correlation between the extracted LCIs and LST was tested using SPSS 16.0 to select the Index that has the highest correlation with LST. After the Index was selected, a linear regression model was developed. As investigated by Mushore et al (2018), the model accuracy to predict LST from UI was assessed using 200 sample points. In the same way, the accuracy was assessed between the LST retrieved from thermal bands and LST calculated from the NDBI using regression model through sample points by Mean Absolute Percentage Error (MAPE).

$$\mathrm{MAPE}(\%) = \frac{1}{N}\sum_{i=1}^{N}\left(\left|\frac{\mathrm{Tpredicted}_i - \mathrm{Tobserved}_i}{\mathrm{Tobserved}_i}\right|\right) * 100 \ldots\ldots\ldots\ldots\ldots\ldots\ldots\ldots\ldots (19)$$

Where,

T*predicted* and T*observed are:* LST computed from NDBI and retrieved from Landsat image

Table 3.10 Interpretation of MAPE values

MAPE (%)	<10	10 – 20	20 – 50	>50
Interpretation	Highly accurate forecasting	Good forecasting	Reasonable forecasting	Inaccurate forecasting

Source: (Lewis, 1982)

3.11 Prediction of Future LULC and LST

3.11.1 Prediction of Future LULC change

Markov Chain develops the transition probability matrix between two different times images(Eastman, 2012a). To accurately model future LULC change(time t+1) from the historical LULC(time t-1) and current LULC(time t), the time of prediction from current should be equal to or less than the time of the first historical map(Arsanjani et al., 2013, Keshtkar et al., 2016). CA uses the transition probability matrices developed from the Markov for the prediction of future change on LULC. Before the prediction LULC changes for 2050, the model was validated using 1991 and 2011 LULC maps to simulate the LULC of 2020. The accuracy was assessed by comparing the classified and simulated maps of 2020. Once validated, the change in LULC was modeled from the 1991 and 2020 LULC maps.

3.11.2 Prediction of future LST

Before predicting LST, correlation analysis was applied between LCI and the LST for the years (1991, 2002, 2011, and 2020). The correlations between LST and LCI was statistically significant for all years. Then, the regression analysis was conducted between NDBI (independent variable) and retrieved LST(dependent variable). For the year 2020, the equation below was formulated.

$$LST = 16.34 * NDBI + 30.07 \ldots \ldots \ldots \ldots \ldots \ldots \ldots \ldots \ldots \ldots \ldots \ldots \ldots \ldots \ldots \ldots .. \ldots \ldots \ldots (20)$$

The retrieved LST maps were categorized into four classes (10 – 20, 20 – 27, 27 – 34, and 34 – 45 ^{0}c). These LST categories were selected solely to assist the relationship of LST distributions between 1991 and 2020. Then, the NDBI maps were categorized into the same four classes so that they could predict each LST category. The classification is mandatory because the CA-Markov predicts a class. Similar to modeling future LULC, which is described in the section above, NDBI of 1991 and 2020 were used as input to the CA-Markov model to predict future NDBI of 2050. Finally, the equation (20) and predicted NDBI of 2050 were used to predict the future LST of the study area for 2050.

CHAPTER 4 RESULTS

4.1 Urban Land Use Land Cover Change between 1991 and 2020

Figure 4.1 shows the spatial distribution of the LULC map of 1991, 2002, 2011, and 2020. Table 4.1 and Figure 4.2 show the statistics of each LULC class for the same years. From 1991 to 2002, the coverage of water bodies, agricultural land, and vegetation area was decreased by 122.76 ha, 5044.86 ha, and 777.89 ha, respectively within 11 years. But, the coverage of the built-up area was increased by 5946.03 ha. From 2002 to 2011, the coverage of the water bodies decreased by a small amount (9.09 ha) while the coverage of the built-up area was increased by 10836.81 ha (highest change). Agricultural land and vegetation areas were decreased by 7383.60 ha and 3444.12 ha, respectively between 2002 and 2011. From the year 2011 to 2020, the built-up area was increased radically by 21217.05 ha while water bodies, agricultural land, and vegetation area were decreased by 42.39 ha, 14476.23 ha, and 6698.43 ha, respectively. The change from 1991 – 2020 showed that the built-up area was increased by 37999.89 ha while water body, agriculture, and vegetation areas were decreased. Specifically, agricultural land was decreased by 26904.69 ha. Similarly, water body and vegetation area were decreased by 174.24 ha and 10920.44 ha, respectively in the last 3 decades.

Table 4.2 shows the rate of urban LULC change between 1991 − 2002, 2002 – 2011, 2011 – 2020, and 1991 – 2020. From 1991 – 2002, the built-up area was changed with the highest rate (6.08%) whilst the vegetation area was changed with the lowest rate(-0.25%). The negative sign indicates the coverage of vegetation area was decreased from 1991 to 2002. Similarly, water bodies and agricultural land were changed by the rate of -3.05 % and -0.48 % between the same years. From the year 2002 – 2011, water bodies, agricultural land, and vegetation area were changed by the rate of -0.42 %, -0.92 %, and -1.38 %, respectively. However, the built-up area was changed with a rate of 8.12 % between the same years. Generally, between 1991 and 2020, the coverage of water body, agricultural land, and vegetation area was decreased and was changed with the rate of -1.64 %, 0.98 %, and -1.32 %, respectively. However, the built-up area was increased by the rate of 14.75 % between the same years.

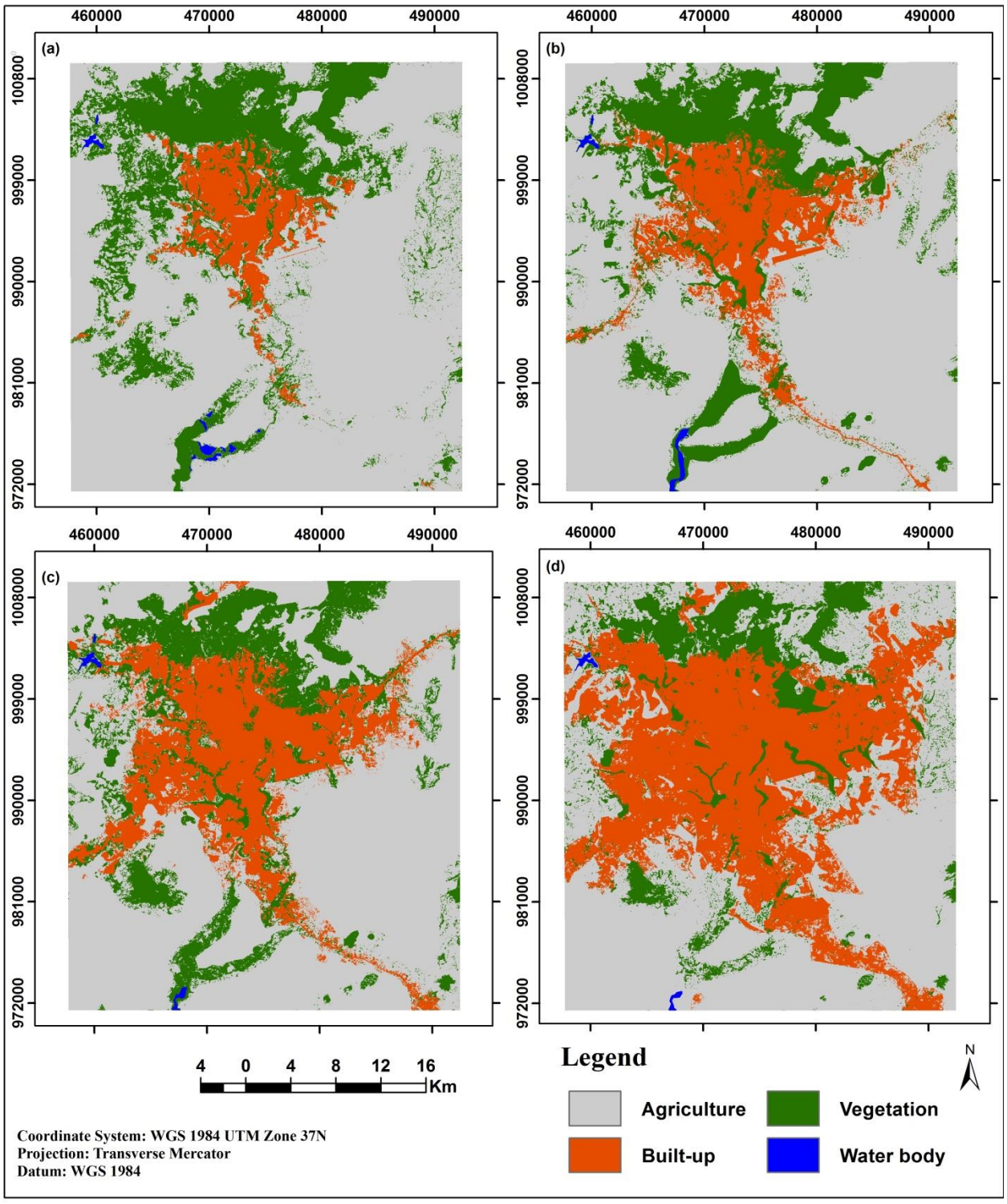

Figure 4.1: LULC maps in (a) 1991, (b) 2002, (c) 2011, and (d) 2020

Table 4.1: Area coverage of LULC between 1991 and 2020

LULC class and area coverage (ha) (1991 – 2020)				
LULC Classes	1991	2002	2011	2020
Waterbody	366.21	243.36	234.27	191.88
Agriculture	94653.72	89608.86	82225.26	67749.03
Vegetation	28464.75	27686.43	24242.31	17543.88
Built-up	8884.44	14830.47	25667.28	46884.33
Total	**132369.1**	**132369.1**	**132369.1**	**132369.1**

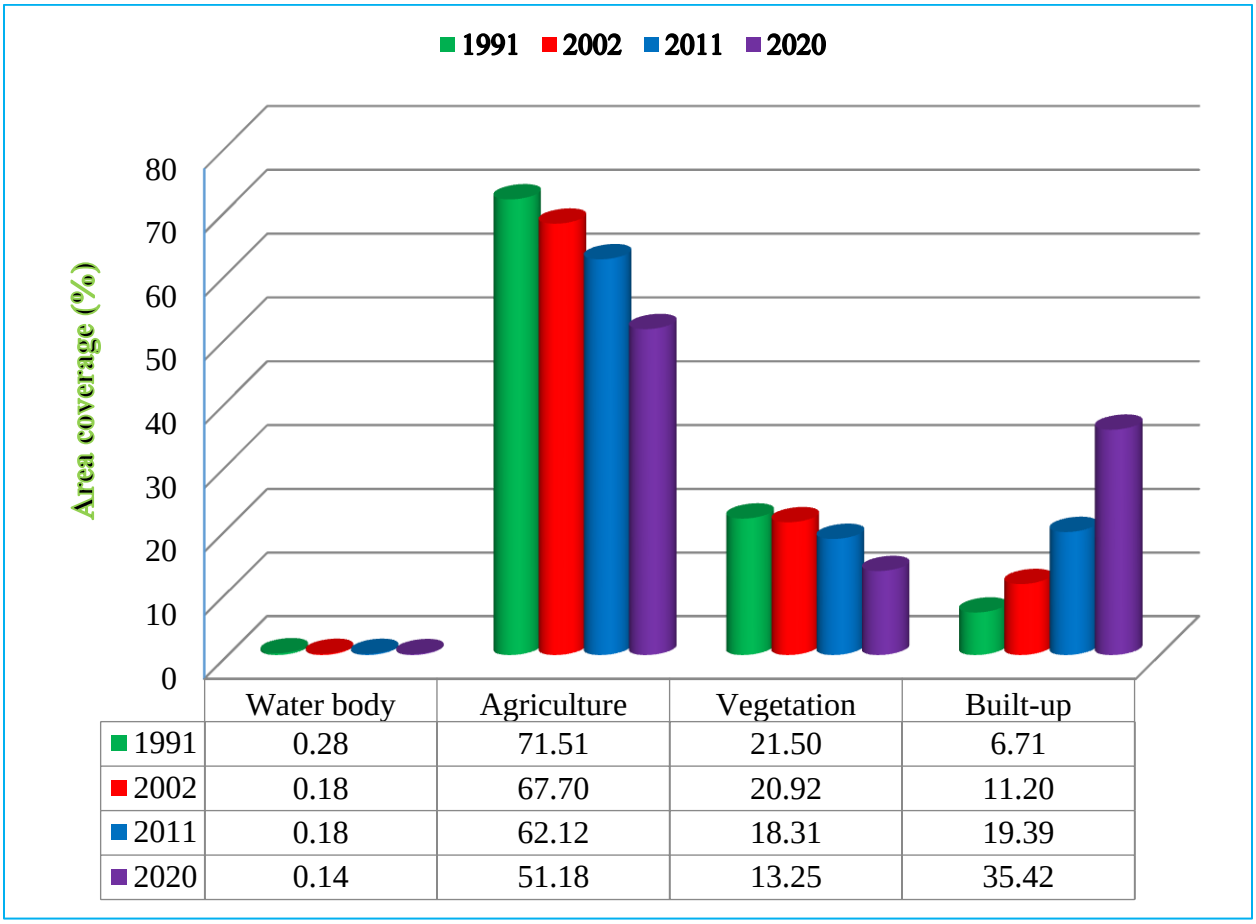

	Water body	Agriculture	Vegetation	Built-up
1991	0.28	71.51	21.50	6.71
2002	0.18	67.70	20.92	11.20
2011	0.18	62.12	18.31	19.39
2020	0.14	51.18	13.25	35.42

Figure 4.2: Area coverage of each LULC in the study area from 1991 to 2020

Table 4.2: Comparison of LULC rate of change from 1991 to 2020

	LULC rate of change (%)			
	1991 – 2002	2002 – 2011	2011 – 2020	1991 – 2020
Waterbody	-3.05	-0.42	-2.01	-1.64
Agriculture	-0.48	-0.92	-1.96	-0.98
Vegetation	-0.25	-1.38	-3.07	-1.32
Built-up	6.08	8.12	9.18	14.75

4.2 Accuracy Assessment of Classified Land Use Land Cover map

The Overall classification accuracy, percentage of user accuracy, producer accuracy, and KIAs are shown in Table 4.3, Table 4.4, Table 4.5, and Table 4.6 for the years 1991, 2002, 2011, and 2020 respectively. The classified LULC map of Addis Ababa city and its surrounding area in 1991 has an overall classification accuracy of 85.25%, and a KIA of 0.80. In 2002, the classified LULC image has the highest overall accuracy (88.75%) and a KIA of 0.88. Similarly, the classified map of 2011 has an overall accuracy of 87.50% and KIA of 0.83. Finally, the classified LULC map of Addis Ababa city and its surrounding area for the year 2020 has an overall classification accuracy of 85.67% and a KIA of 0.81.

Table 4.3: Error matrix for 1991

		Reference (1991)					
	Classified Data	Waterbody	Agriculture	Vegetation	Built-up	Total	UAC (%)
Classified (1991)	Waterbody	91	4	3	0	98	92.86
	Agriculture	0	105	12	7	127	84.68
	Vegetation	2	9	87	19	117	74.36
	Built-up	0	2	1	58	61	95.0
	Total	93	120	103	84	400	
	PAC (%)	97.85	87.50	84.47	69.05		
				Overall Classification Accuracy = 85.25%			
				KIA = 0.80			

Note: PAC = Producer Accuracy and UAC = User Accuracy

Table 4.4: Error matrix for 2002

		Reference (2002)					
	Classified Data	Waterbody	Agriculture	Vegetation	Built-up	Total	UAC (%)
Classified (2002)	Waterbody	86	3	5	4	98	87.76
	Agriculture	1	93	3	2	99	93.94
	Vegetation	5	1	97	11	114	85.09
	Built-up	5	3	2	79	89	88.76
	Total	97	100	107	96	400	
	PAC (%)	88.66	93.00	90.65	82.25		
	Overall Classification Accuracy = 88.75%						
	KIA = 0.85						

Note: PAC = Producer Accuracy, UAC = User Accuracy

Table 4.5: Error matrix for 2011

		Reference Data(2011)					
	Classified Data	Waterbody	Agriculture	Vegetation	Built-up	Total	UAC (%)
Classified Data (2011)	Waterbody	47	2	1	1	51	92.16%
	Agriculture	3	135	4	6	148	91.22%
	Vegetation	0	22	84	6	112	75.00%
	Built-up	0	4	1	84	89	94.38%
	Total	50	163	90	97	400	
	PAC (%)	94.00	82.82	93.33	86.60		
	Overall Classification Accuracy = 87.50%						
	KIA = 0.83						

Note: PAC = Producer Accuracy,

UAC = User Accuracy

Table 4.6: Error matrix for 2020

		Reference Data(2020)					
	Classified Data	Waterbody	Agriculture	Vegetation	Built-up	Total	UAC (%)
Classified Data (2020)	Waterbody	68	0	0	0	68	100.00
	Agriculture	7	86	3	20	116	74.14
	Vegetation	0	8	52	1	61	85.25
	Built-up	0	2	2	51	55	92.73
	Total	75	96	57	72	300	
	PAC (%)	90.67	89.58	91.23	70.83		
	Overall Classification Accuracy = 85.67%						
	KIA = 0.81						

Note: PAC = Producer Accuracy, UAC = User Accuracy

4.3 Land Use Land Cover Change Detection

Table 4.7 shows the change from each LULC class to all LULC classes between two different years (1991 – 2002, 2002 – 2011, 2011 – 2020, and 1991 – 2020). The diagonal elements in each period show the area covered during the transition of each LULC class to itself or unchanged. Between 1991 and 2002, 83076.39 ha of agricultural land were unchanged. Similarly, 214.21 ha of the waterbody, 20372.59 ha of vegetation area, and 8821.26 ha of the built-up area remain in their class between 1991 and 2002. On the other hand, the off-diagonal elements in Table 4.7 represent the change that occurred from each LULC class to other LULC classes. From 1991 – 2002), 10.89 ha, 7117.56 ha, and 4448.88 ha of agricultural land were changed to a water body, vegetation, and built-up area, respectively. The larger area was transformed between agricultural land and vegetation area throughout the study period. The net changes and the gains and losses for each category between 199 – 2002, 2002 – 2011, 2011 – 2020, and 1991 – 2020 are shown in appendix 1

Table 4.7: Change detection matrix from 1991 to 2020

	Area coverage (km^2)			
	1991 – 2002			
	Waterbody	**Agriculture**	**Vegetation**	**Built-up**
Waterbody	**2.14**	0.11	0.18	0
Agriculture	0.47	**830.76**	65.14	0.14
Vegetation	1.47	71.18	**203.73**	0.49
Built-up	0	44.49	15.60	**88.21**
	2002 – 2011			
Waterbody	**2.26**	0.03	0.05	0
Agriculture	0.02	**775.37**	46.68	0.18
Vegetation	0.15	41.15	**200.86**	0.25
Built-up	0	79.53	29.27	**147.87**
	2011 – 2020			
Waterbody	**1.79**	0.01	0.07	0
Agriculture	0.35	**625.67**	51.31	0.15
Vegetation	0	33.61	**141.75**	0.07
Built-up	0.15	162.95	49.28	**246.61**
	1991 – 2020			
Waterbody	**0.96**	0.07	0.88	0
Agriculture	1.27	**612.59**	63.62	0
Vegetation	1.28	41.93	**132.22**	0
Built-up	0.14	291.94	87.92	**88.84**

4.4 Land Cover Indices

4.4.1 Normalized Difference Vegetation Index

Figure 4.3 indicates the NDVI map of the study area between 1991 and 2020. In 2002, the highest NDVI value (0.87) and in 2020, the lowest NDVI value (-0.88) were observed. The values of NDVI ranges from (-0.46 – 0.74), (-0.59 – 0.87), (-0.53 – 0.76), and (-0.88 – 0.73) in

1991, 2002, 2011, and 2020, respectively. Table 4.8 shows the minimum, mean, and maximum values of NDVI.

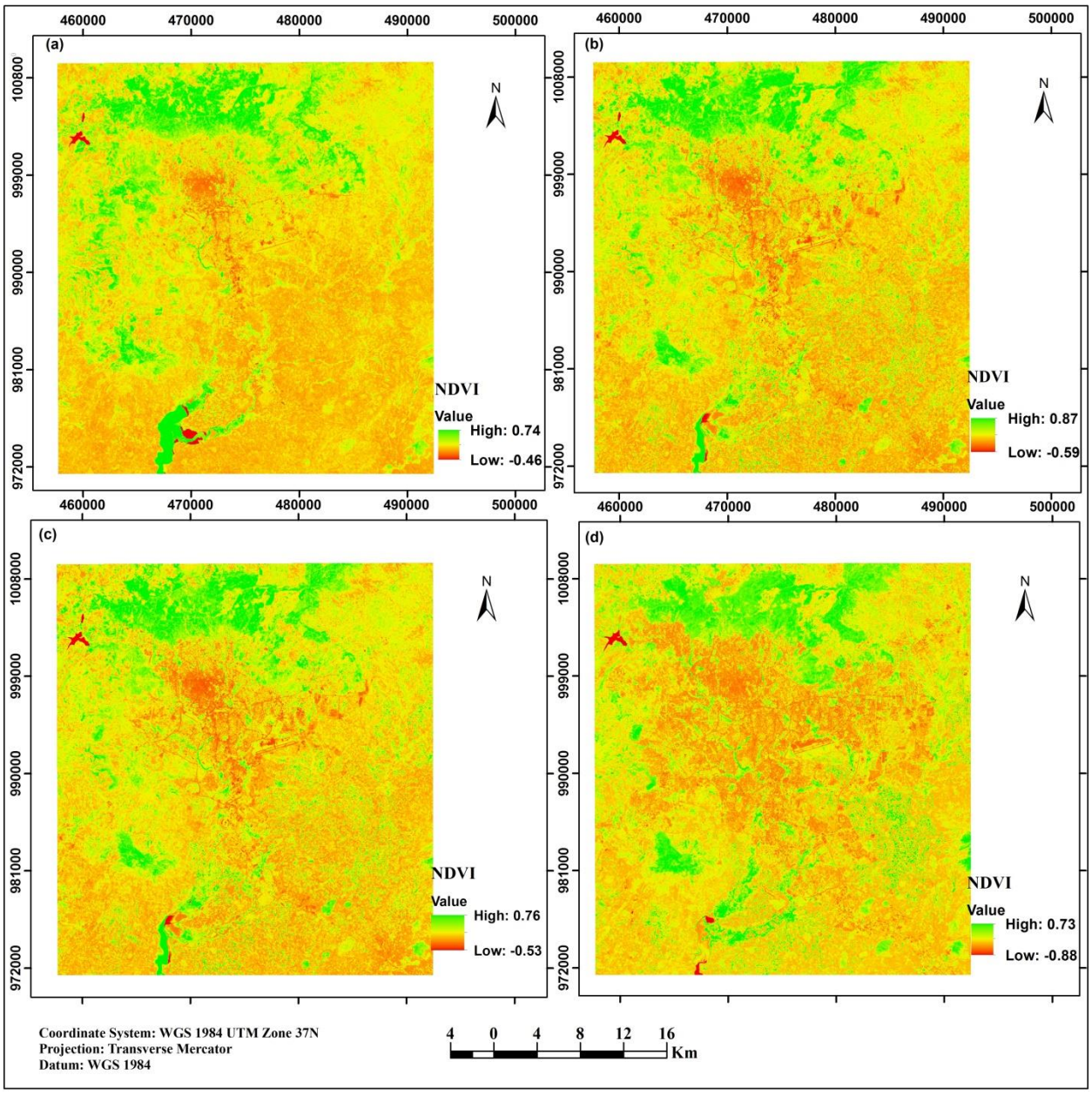

Figure 4.3: NDVI Maps for the years (a) 1991, (b) 2002, (c) 2011, and (d) 2020

The year 2002 has the highest mean NDVI (0.24) while 2020 has the lowest mean NDVI (0.04). On the other hand, 1991 and 2011 have a mean NDVI of 0.14 and 0.17, respectively. From Figure 4.4, the trend of the minimum, mean, and maximum values of NDVI values show decreasing from the year 1991 to 2020. Exceptionally, between 1991 and 2002 the graph shows an increasing trend.

Table 4.8: Min, Mean, and Max values of NDVI between 1991 and 2020

Time	Minimum	Mean	Maximum
1991	-0.46	0.14	0.74
2002	-0.59	0.24	0.87
2011	-0.53	0.17	0.76
2020	-0.88	0.04	0.73

Min - minimum and Max - maximum

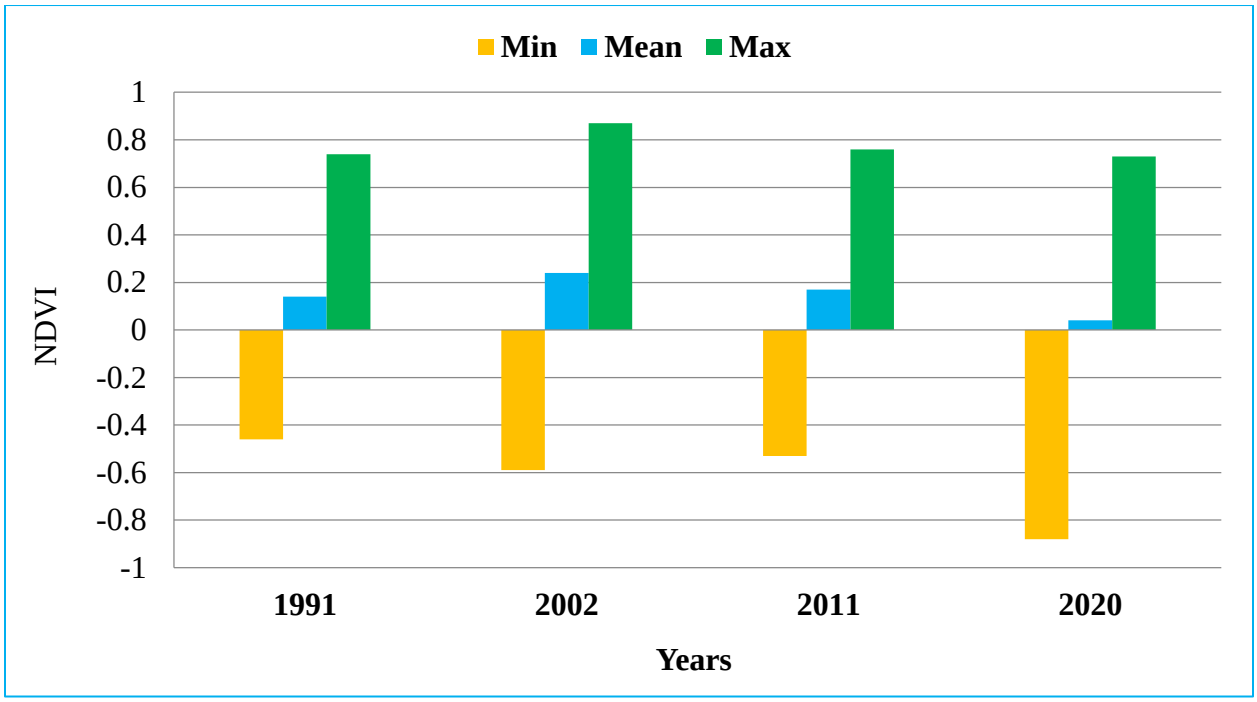

Figure 4.4: The minimum, mean, and maximum values of NDVI in different years

4.4.2 Normalized Difference Built-Up Index

Figure 4.5 shows the NDBI maps in 1991, 2002, 2011, and 2020. In contrary to NDVI, an area covered by healthy and green vegetation has lower NDBI values. The year 2020 has the highest NDBI value (0.93) and 2002 has the lowest NDBI value (-0.83). The year 1991 has a minimum NDBI value of -0.63 and a maximum value of 0.57. Similarly, in 2011, -0.71 and 0.49 minimum and maximum values of NDBI were observed.

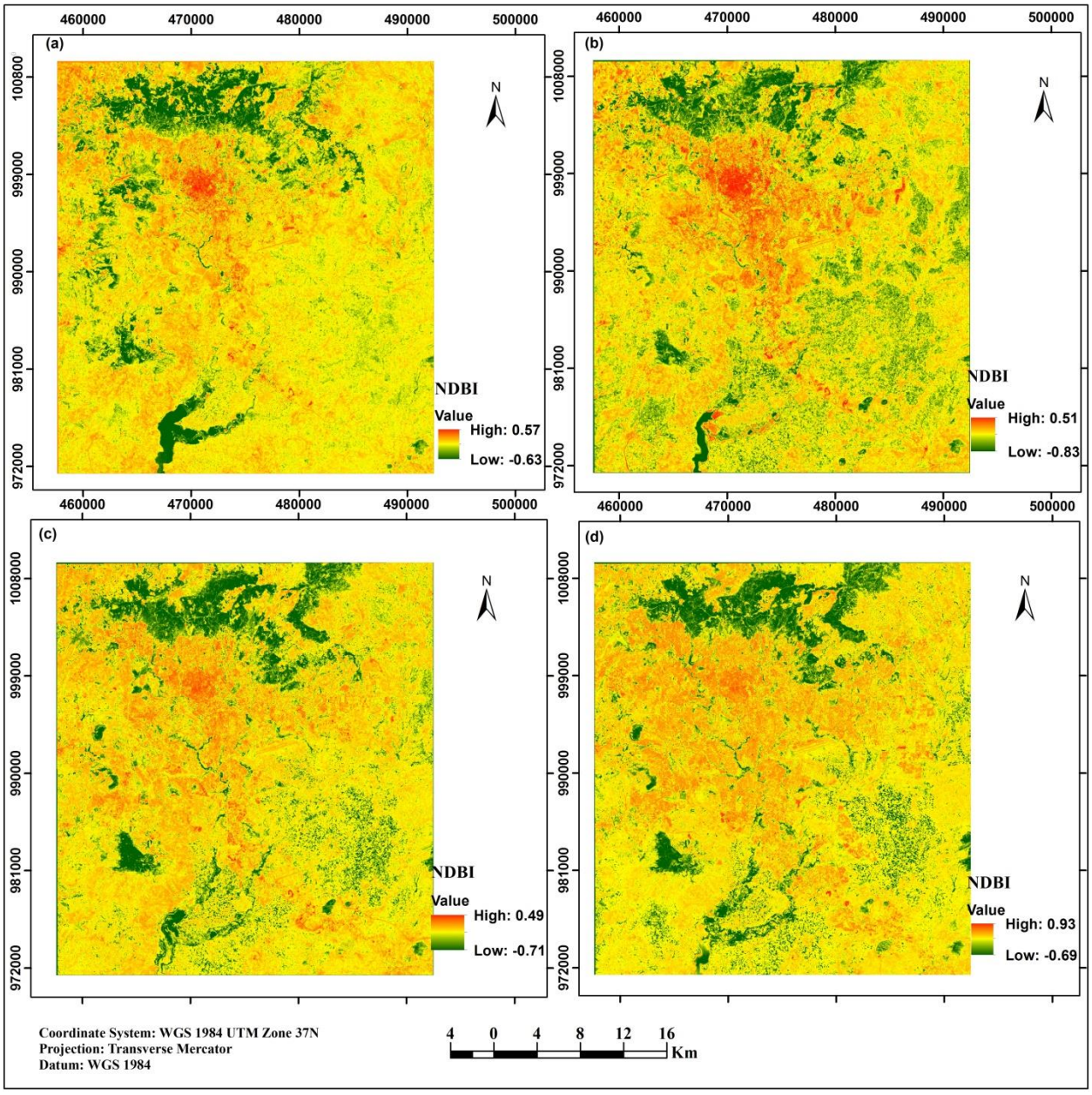

Figure 4.5: NDBI maps in (a) 1991, (b) 2002, (c) 2011, and (d) 2020

4.4.3 Soil Adjusted Vegetation Index

Figure 4.6 shows the SAVI maps at different years. Similar to NDVI, green vegetation has higher SAVI values when compared to other LULC. Higher values of SAVI were observed in both 1991 (0.74) and 2020 (0.75) over areas covered by green vegetation. On the other hand, the lowest SAVI value (-0.68) was observed in 1991.

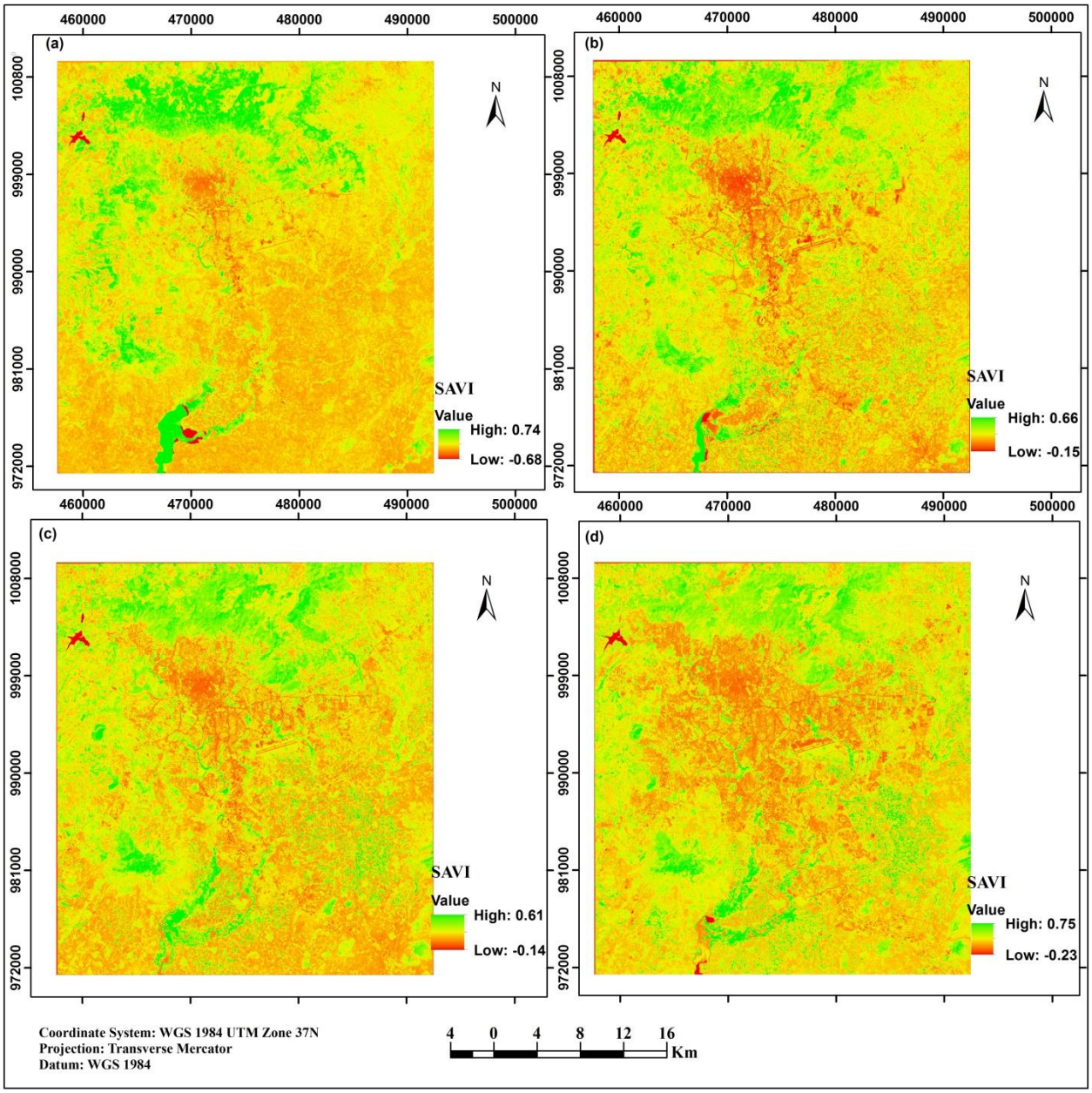

Figure 4.6: SAVI maps in (a) 1991, (b) 2002, (c) 2011, and (d) 2020

4.4.4 Urban Index

Figure 4.7 shows four UI maps between 1991 and 2020. The highest value of UI (0.92) was observed in 2020 and the lowest value of UI (-0.87) was observed in 2002. In the years 1991, 2002, 2011, and 2020, the maximum values of UI observed were 0.47, 0.56, 0.49, and 0.92 and the minimum values of UI observed were -0.81, -0.87, -0.77, and -0.83, respectively.

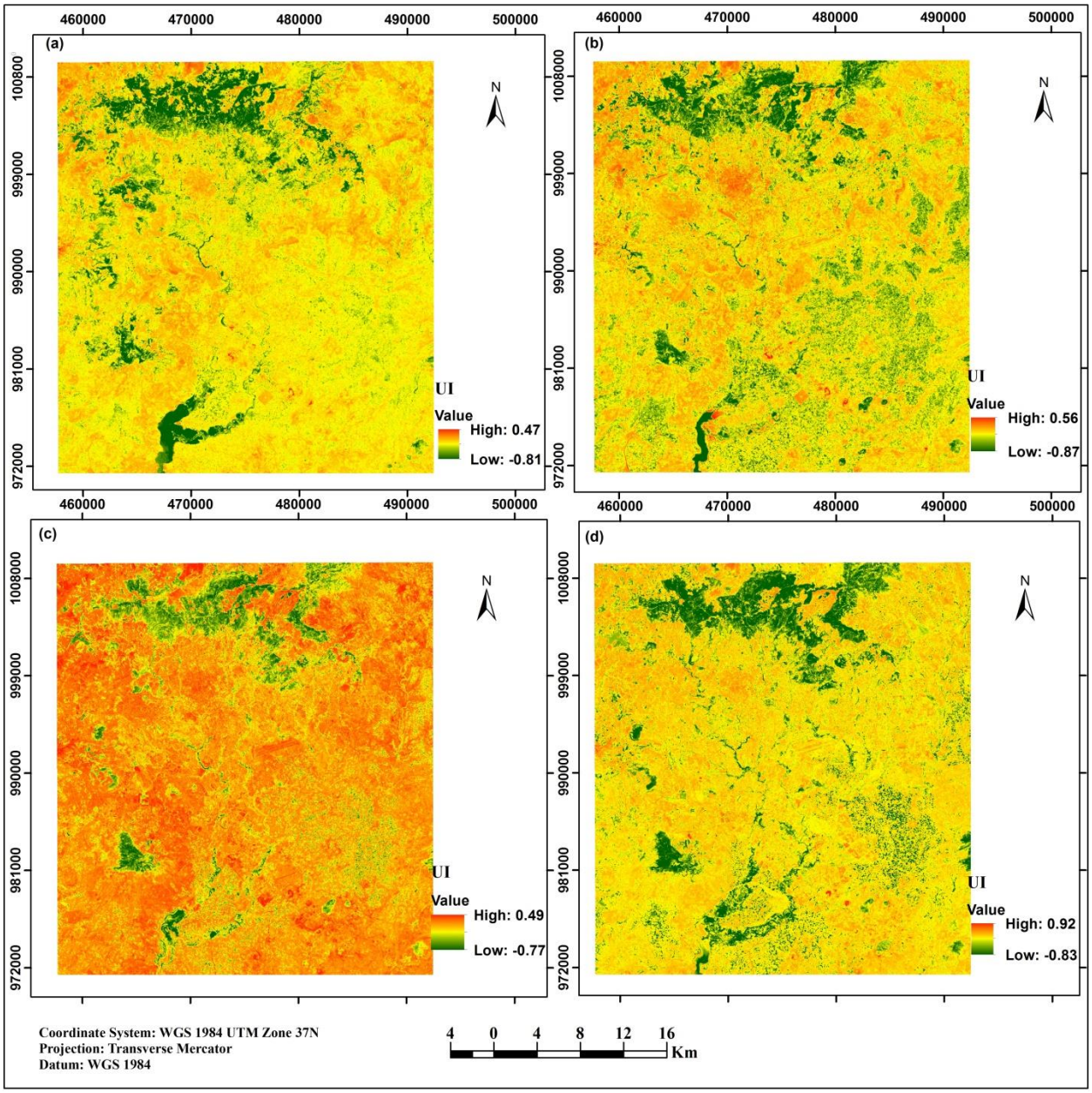

Figure 4.7: UI maps in (a) 1991, (b) 2002, (c) 2011, and (d) 2020

4.5 Land Surface Temperature Distribution between 1991 and 2020

Figure 4.8 shows the minimum, mean, and maximum LST observed in the years 1991, 2002, 2011, and 2020. The highest mean LST was observed in 2020 with 30.32 ^{0}c and the lowest mean LST was observed in 1991 with 22.92 ^{0}c. On the other hand, the observed mean LST in 2002 and 2011 were 28.39 ^{0}c and 26.78 ^{0}c, respectively. Maximum LSTs observed in 1991, 2002, 2011, and 2020 were 32.99 ^{0}c, 39.55 ^{0}c, 36.97 ^{0}c, and 40.72 ^{0}c, respectively. In 2002, higher mean LST was observed than in 1991 and 2011. The minimum, mean, and maximum values of LST showed an increasing trend from 1991 to 2020 (Figure 4.8).

Figure 4.9 shows the spatial distribution of four LST categories of the study area in 1991, 2002, 2011, and 2020. The area coverage of the lowest category (10 – 20 ^{0}c) was decreased from 12.31% in 1991 to 1.19% in 2020. The highest category (34 – 45 ^{0}c) was increased from 0% in 1991 to 12.08% in 2020. In 1991, 81.73% of the total area was found under the second category (20 – 27 ^{0}c). But, in 2002, 2011, and 2020 the third category (27 – 34 ^{0}c) has a maximum area coverage of 70.20%, 55.03%, and 75.16% of the total area, respectively. The detailed statistics of each LST category for the year (1991 to 2020) are shown in Table 4.9 and figure 4.10.

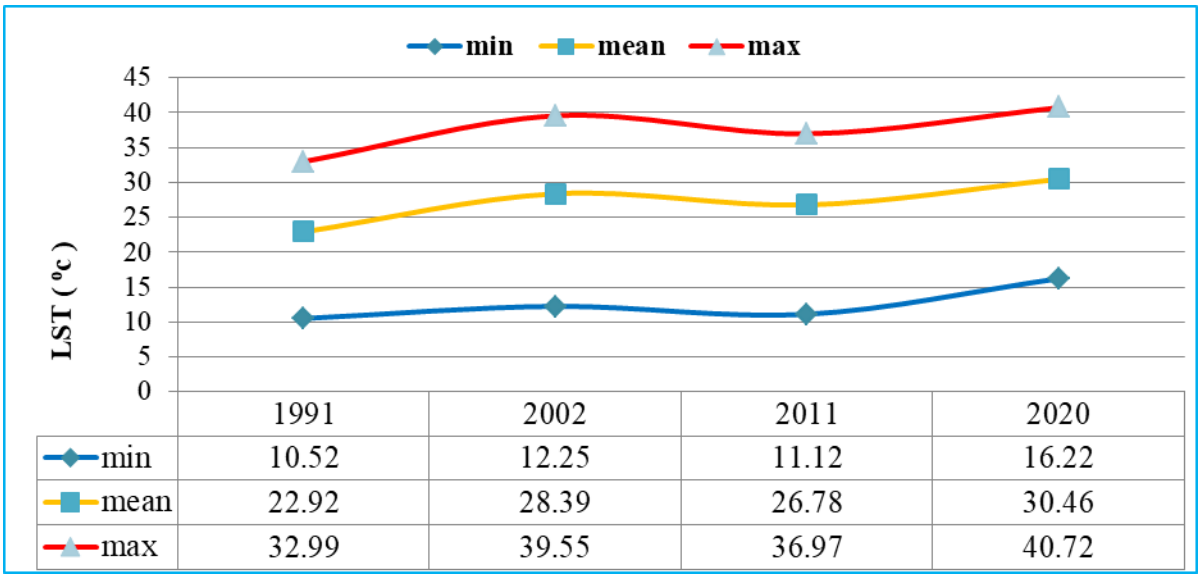

	1991	2002	2011	2020
min	10.52	12.25	11.12	16.22
mean	22.92	28.39	26.78	30.46
max	32.99	39.55	36.97	40.72

Figure 4.8 Minimum, mean, and maximum LST in 1991, 2002, 2011, and 2020

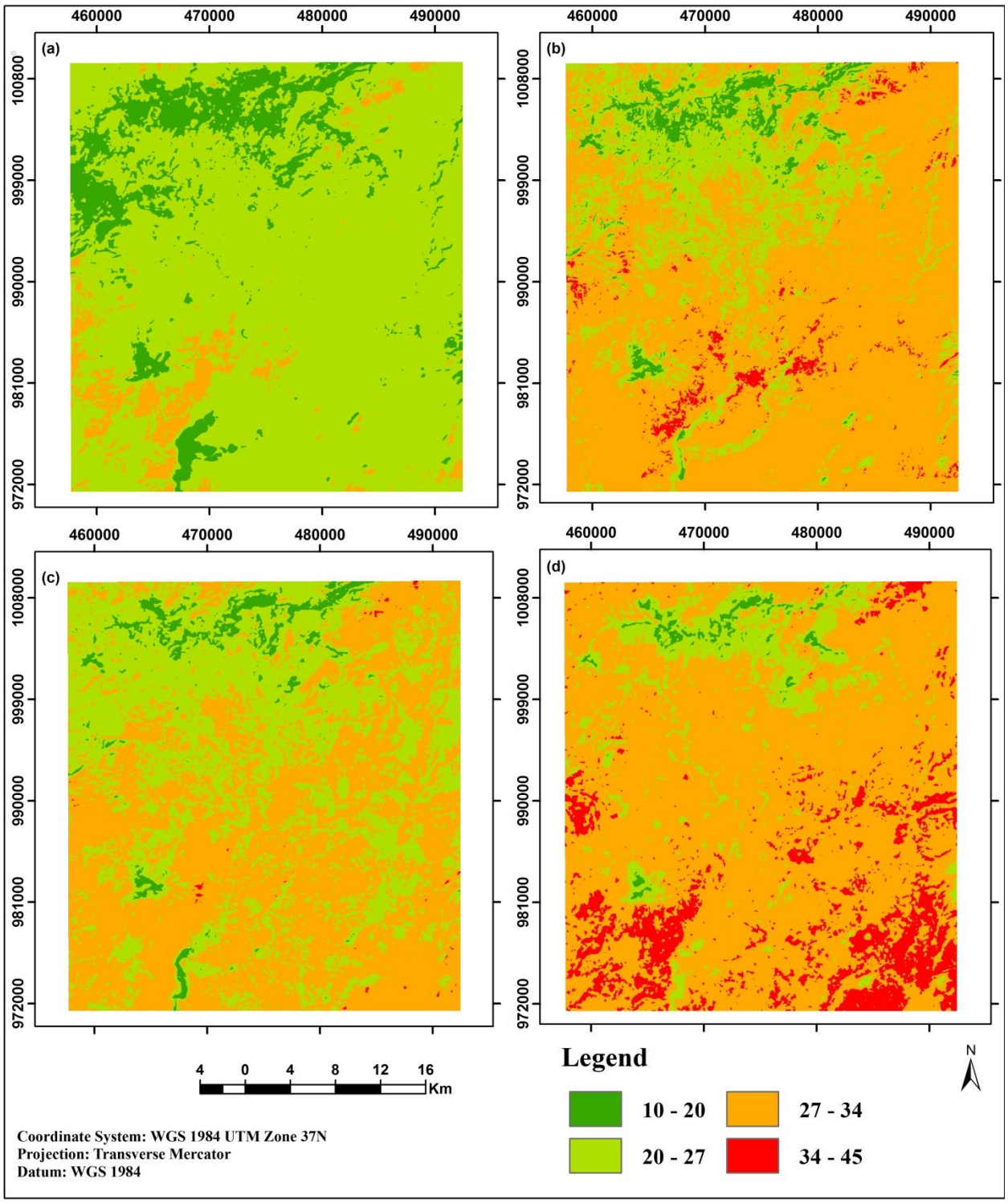

Figure 4.9: LST maps for the years a) 1991, b) 2002, c) 2011, and d) 2020

Table 4.9: Area coverage of LST categories from 1991 to 2020

LST area coverage (ha) in different years				
LST class	1991	2002	2011	2020
10 - 20	16247.32	4976.05	4207.54	1518.88
20 - 27	108226	31431.8	55105.2	15320.00
27 - 34	7895.79	92961.7	72874.8	99479.02
34 - 45	0.00	2999.52	181.53	16051.20
Total	**132369.1**	**132369.1**	**132369.1**	**132369.1**

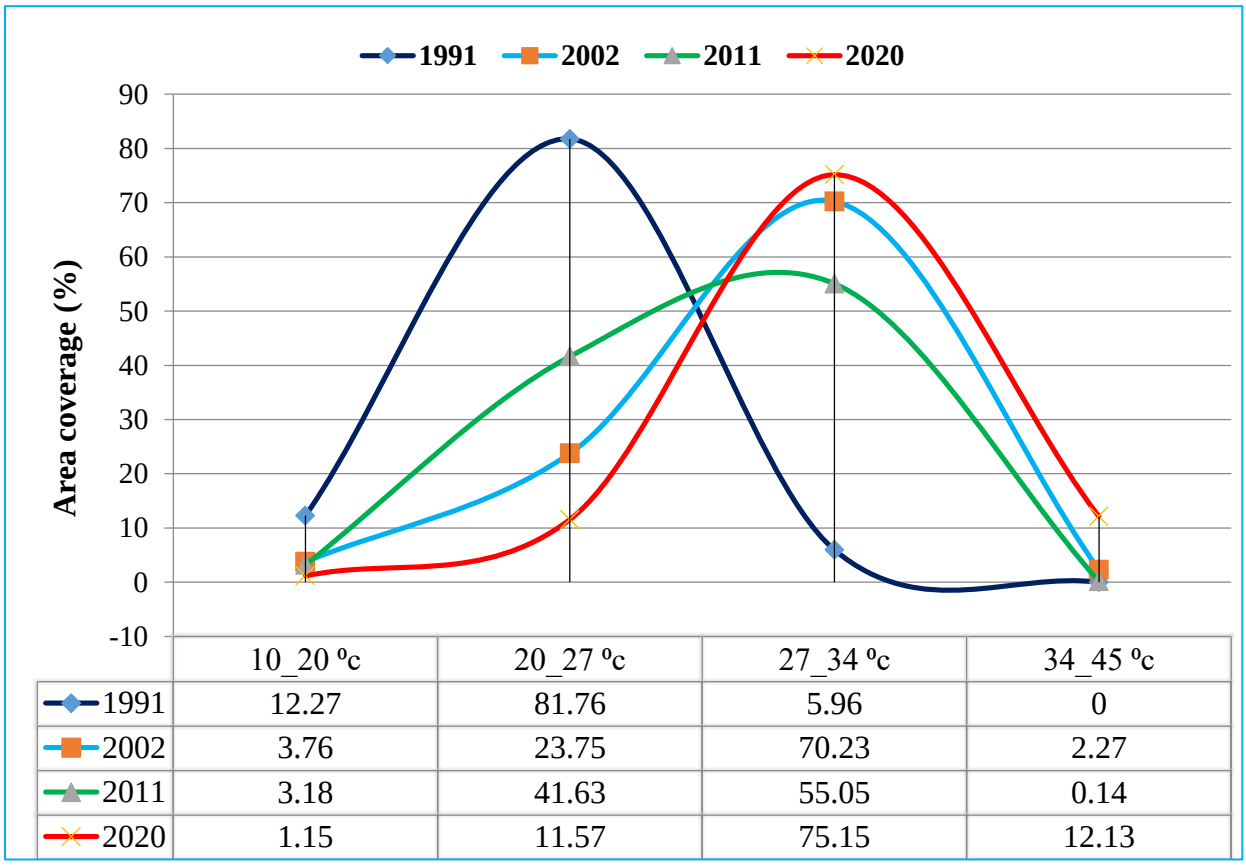

	10_20 ºc	20_27 ºc	27_34 ºc	34_45 ºc
1991	12.27	81.76	5.96	0
2002	3.76	23.75	70.23	2.27
2011	3.18	41.63	55.05	0.14
2020	1.15	11.57	75.15	12.13

Figure 4.10: Area coverage (%) of LST categories in different years

4.6 Selection of Land Cover Indices

4.6.1 Correlation between LCI and LST

Figure 4.9 shows the relationships between LST and four LCI (NDVI, NDBI, SAVI, and UI) for the year 2020. NDBI has stronger positive correlation with LST ($R^2 = 0.52$, $p < 0.05$) and UI has weaker correlation with LST ($R^2 = 0.23$, $p < 0.05$) when compared to other LCI. On the other hand, NDVI and SAVI have negative relationships with LST. NDVI has a weaker correlation with LST than NDBI ($R^2 = 0.34$, $p < 0.05$).

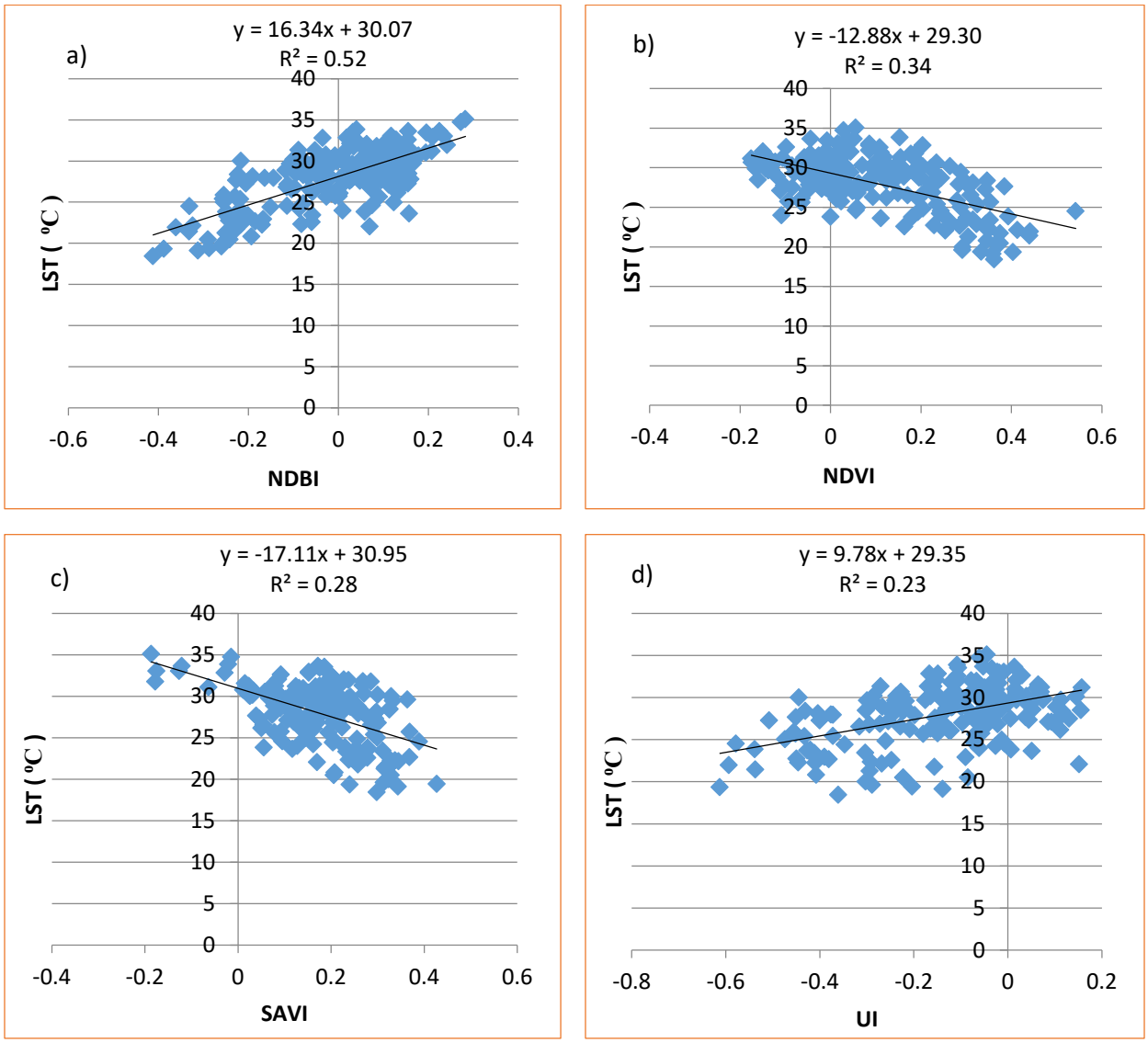

Figure 4.11. Correlation between LST and LCI for 2020

NDBI is strongly correlated with LST than other LCI and was the best predictor of LST ($R = 0.72$, $p < 0.05$ in 1991 and 2020 and $R = 0.71$, $p < 0.05$ in 2002, and 2011) (Table 4.10 and 4.11) when compared to other indices. The sign of the coefficient identifies whether LCI and LST are positively or negatively correlated and the magnitude identifies the strength of relationships. Table 4.10 shows the correlation between LCI and LST for the years 2011 and 2020 and Table 4.11 shows the correlation between LCI and LST for 1991 and 2002.

Table 4.10: Correlation between LCI and LST in 2020 and 2011

	2020					2011				
	UI	SAVI	NDVI	NDBI	LST	UI	SAVI	NDVI	NDBI	LST
UI	1					1				
SAVI	-0.56	1				-0.60	1			
NDVI	-0.77	0.58	1			-0.72	0.60	1		
NDBI	0.83	-0.58	-0.75	1		0.85	-0.61	-0.76	1	
LST	0.48	-0.53	-0.58	0.72	1	0.45	-0.52	-0.57	0.71	1

Table 4.11: Correlation between LCI and LST in 2002 and 1991

	2002					1991				
	UI	SAVI	NDVI	NDBI	LST	UI	SAVI	NDVI	NDBI	LST
UI	1					1				
SAVI	-0.57	1				-0.53	1			
NDVI	-0.76	0.56	1			-0.74	-0.58	1		
NDBI	0.85	-0.60	-0.73	1		0.82	-0.60	-0.71	1	
LST	0.48	-0.54	-0.56	0.71	1	0.46	-0.52	-0.56	0.72	1

4.6.2 Accuracy of LST Retrievals Using NDBI

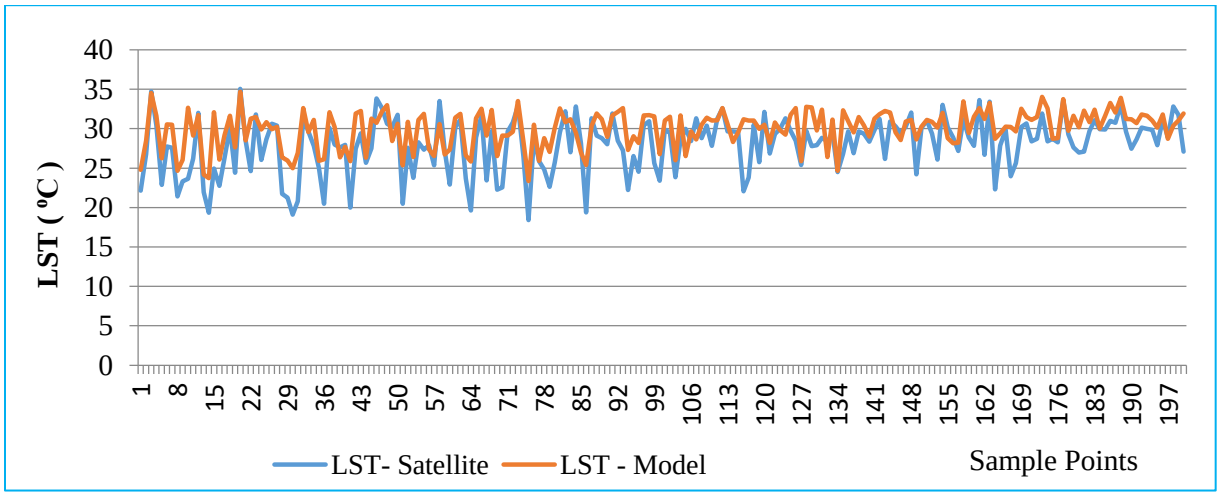

Figure 4.12: Comparison of LST derived from Landsat data computed from the NDBI

The accuracy of estimating the LST using the regression model was assessed by comparing the LST retrieved from thermal bands of Landsat images and the LST calculated from NDBI using the regression equation. Using sample points, the accuracy was checked and has a Mean Absolute Percentage Error (MAPE) of 9.40 %, Index of agreement of 0.71, and the Root Mean Square Error of 3.08 ^{0}C. From these results, predicting LST from NDBI is highly accurate using a regression model.

4.7 Land Use Land Cover Modeling

Table 4.12 and 4.13 shows the transition probability matrix between 1991 – 2011 and 1991 – 2020, respectively. The diagonal elements in the matrix show the probability of each LULC change to the same class. From Table 4.12, the built-up area has the highest probability (0.84) to be unchanged from 1991 to 2011. On the other hand, vegetation area has a lower probability (0.62) to be unchanged when compared to other LULC between 1991 and 2011. The off-diagonal elements specify the probability of changing from the existing classes to new classes between specified times. Between the years 1991 and 2011, vegetation area has a higher probability (0.27) of changing to agricultural land. Agricultural land and vegetation area have comparable probability (0.17) and (0.14) of changing to built-up, respectively. The Markovian conditional probability maps of predicted LULC 2020 and 2050 are shown in Appendix 2 and 3, respectively.

Table 4.12. Transition probability matrix for the prediction of 2020 LULC

		2011			
	Class Name	Waterbody	Agriculture	Vegetation	Built-up
1991	Water body	**0.7906**	0.0188	0.1906	0.0000
	Agriculture	0.0001	**0.7355**	0.0902	0.1743
	vegetation	0.0003	0.2354	**0.6167**	0.1476
	Built-up	0.0000	0.0630	0.0894	**0.8475**

Table 4.13. Transition probability matrix for the prediction of 2020 LULC

		2020			
	Class Name	Waterbody	Agriculture	Vegetation	Built-up
1991	Water body	**0.1538**	0.4285	0.4023	0.0154
	Agriculture	0.0001	**0.6081**	0.0532	0.3385
	vegetation	0.0035	0.273	**0.3825**	0.3409
	Built-up	0.0000	0.0001	0.0000	**0.9999**

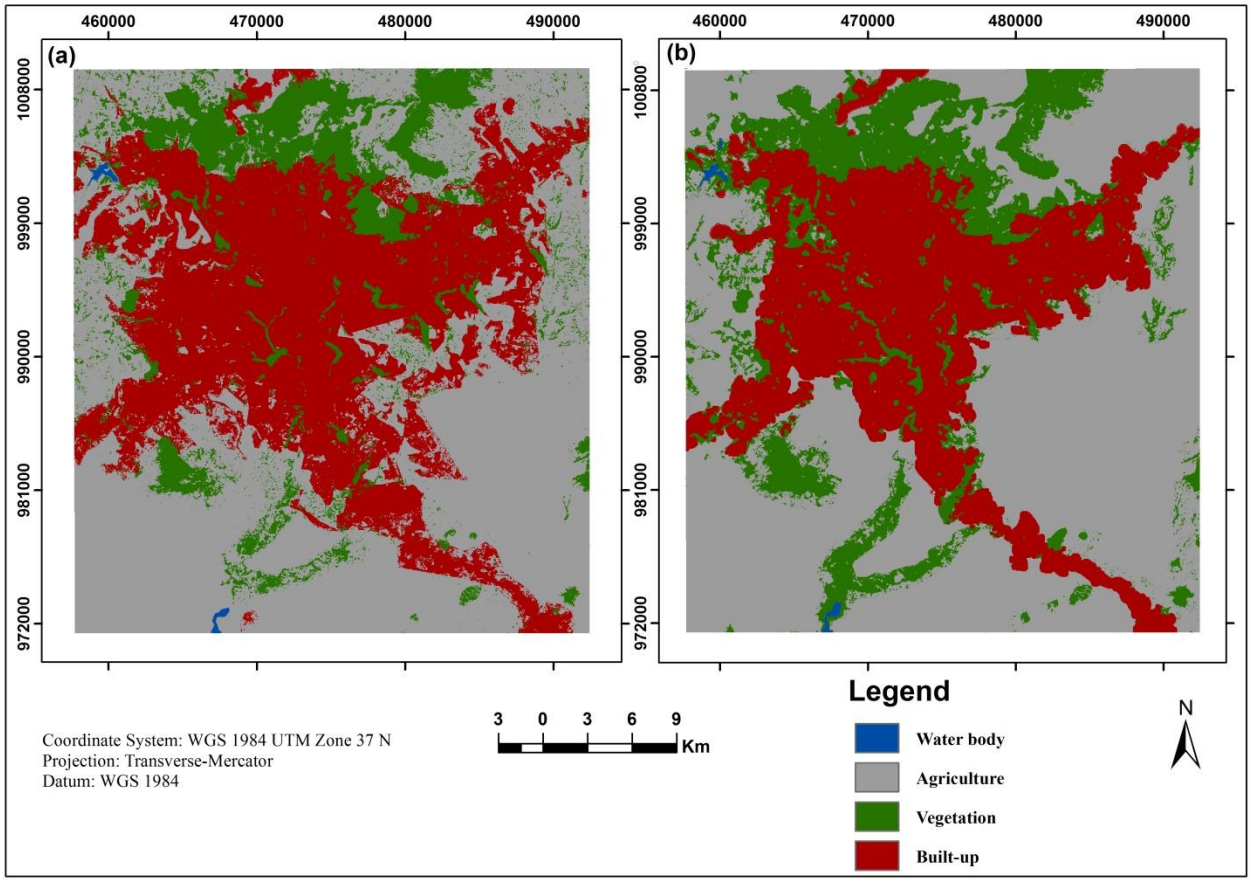

Figure 4.13: LULC Map of a) Classified and b) Predicted for 2020

Table 4.14 shows the comparison of LULC classes area coverage between classified and simulated maps of 2020. Each LULC classes of the two maps have comparable area coverage. For example; the area covered by the water body in the classified map was 191.88 ha and 214.20 ha in the simulated map for the year 2020. On the other hand, the actual and simulated areal coverage of the built-up area was 46884.33 and 36867.42 ha respectively. The simulated built-up area coverage was lower than the actual built-up area for 2020.

Table 4.14: Areal Coverage of Classified and Simulated LULC of 2020

Class Name	Classified Area (ha)	Simulated Area (ha)
Built-up	46884.33	36867.42
Vegetation	17543.88	22527.63
Agriculture	67749.03	72759.87
Waterbody	191.88	214.20

4.7.1 Validation of the Model

Table 4.15 shows KIA values for each LULC category obtained during validation. The KIA between the simulated LULC map and the classified LULC map for 2020 was 0.70. the built-up area has the strongest similarity (KIA = 0.98) and the waterbody has the weakest similarity (KIA = 0.62) between simulated and classified LULC maps of 2020. Vegetation areas and agricultural land have a substantial strength of similarity (KIA = 0.76) between the simulated and classified maps of the same year. Using the classified map of 2020 as a reference, the simulated map matched with the classified map with an accuracy of 82.18 %. From the result obtained, it was possible to proceed to predict the future LULC of 2050.

Table 4.15: KIA of each LULC classes

LULC Class	Built-up	Vegetation	Agriculture	Waterbody
KIA	0.98	0.76	0.76	0.62

4.8 Future LULC and LST for 2050

4.8.1 Prediction of future LULC for 2050

Figure 4.15 shows the predicted LULC map of the study area for the year 2050. In the next 3 decades, the built-up area coverage was predicted to increase by 26013.2 ha. But, the coverage of waterbody, agricultural land, and vegetation area was predicted to decrease by 16.36 ha, 19133.17 ha, and 6863.65 ha, respectively. Table 4.16 and Figure 4.14 show the comparison of the area coverage of each LULC class between 2020 and 2050.

Table 4.16: Area coverage of each LULC classes in 2020 and 2050

LULC Classes	LULC Area coverage in ha	
	2020	2050
Waterbody	191.88	175.52
Agriculture	67749.03	48615.86
Vegetation	17543.88	10680.23
Built-up	46884.33	72897.5
Total	**132369.1**	**132369.1**

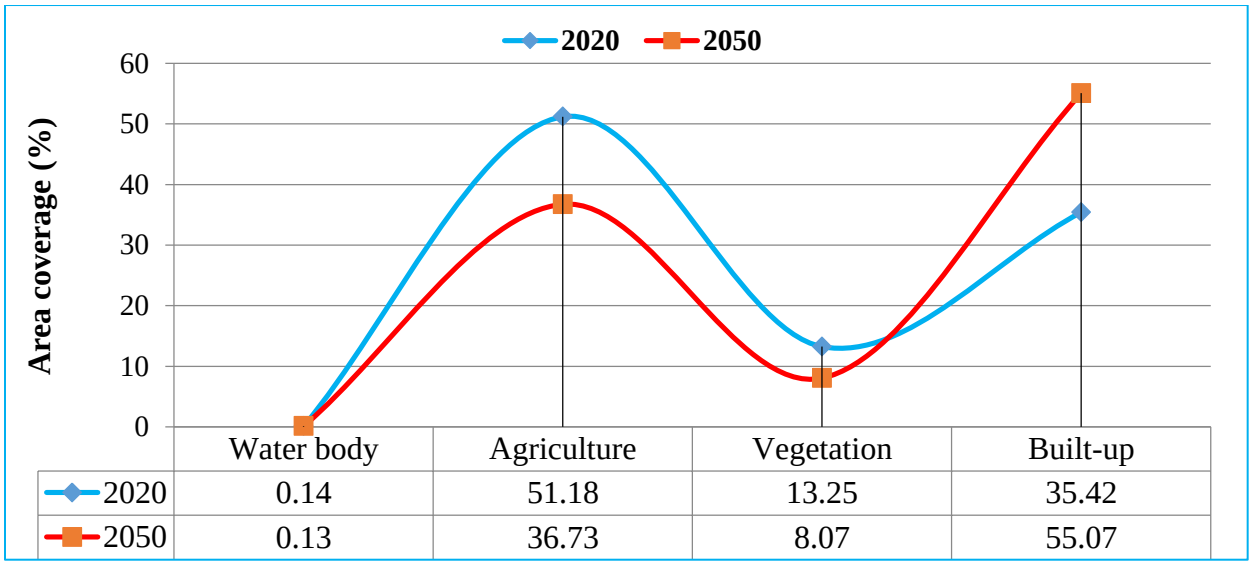

Figure 4.14: Comparison of LULC area coverage between 2020 and 2050

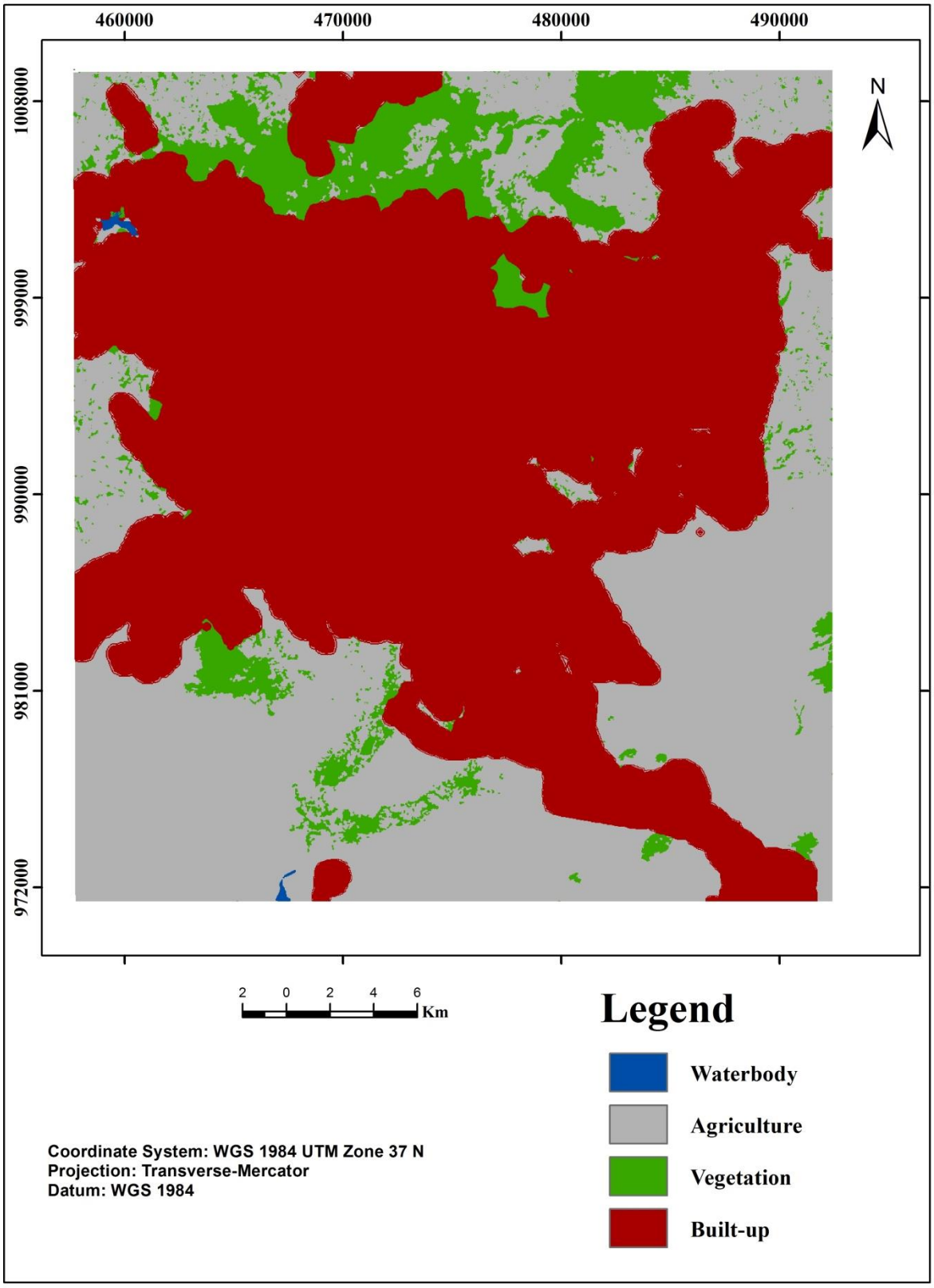

Figure 4.15. Predicted LULC Map of the study area for the year 2050

4.8.2 Prediction of Future LST for 2050

Figure 4.17 shows the predicted LST map of the study area for the year 2050. The area covered by the lower LST category (10 – 20 ^{0}c) was predicted to decrease while the area covered by the highest LST category (> 34 ^{0}c) was predicted to increase. The area covered by the first three LST categories (10 – 20 ^{0}c, 20 – 27 ^{0}c, and 27 – 34 ^{0}c) was predicted to decrease by 543.78 ha, 2,707.59 ha, and 101.92 ha respectively. Contrary to the lower categories, the area covered by the highest category (34 – 45 ^{0}c) was predicted to increase by 3,353.29 ha from 2020 to 2050. Table 4.17 and figure 4.16 show the comparison of the area covered by each LST category between 2020 and 2050. The classified and the predicted maps of NDBI are shown in Appendix 4 and 5.

Table 4.17: Area coverage of LST Categories in 2020 and 2050

	Area coverage of LST categories in ha	
LST Class	2020	2050
10 – 20 ^{0}C	1518.88	975.10
20 – 27 ^{0}C	15320.00	12,612.41
27 – 34 ^{0}C	99479.02	99,377.10
34 – 45 ^{0}C	16051.20	19,404.49
Total	**132369.1**	**132369.1**

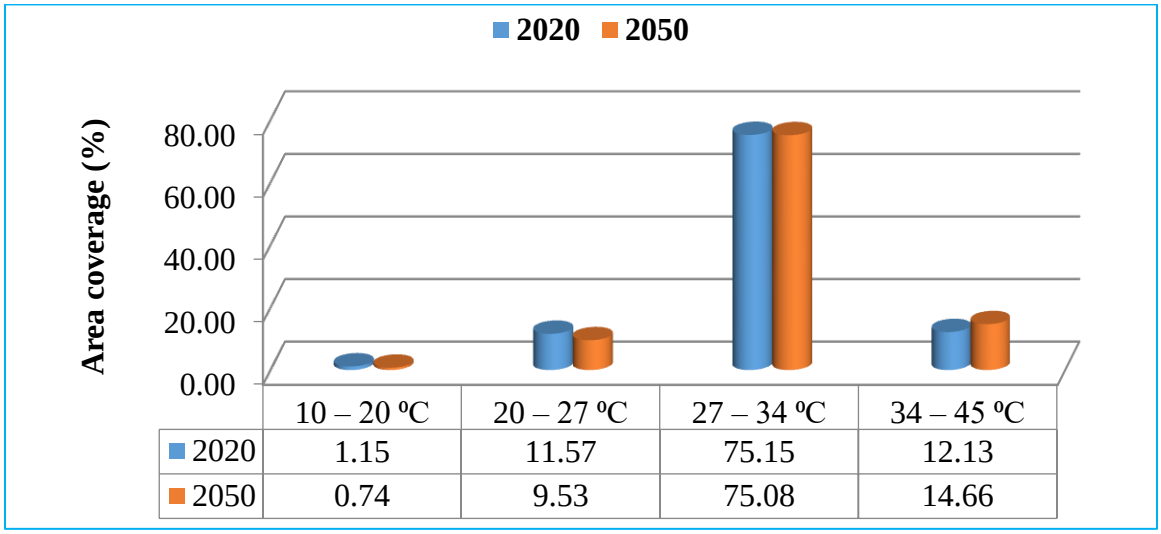

Figure 4.16: Comparison of area coverage of LST categories between 2020 and 2050

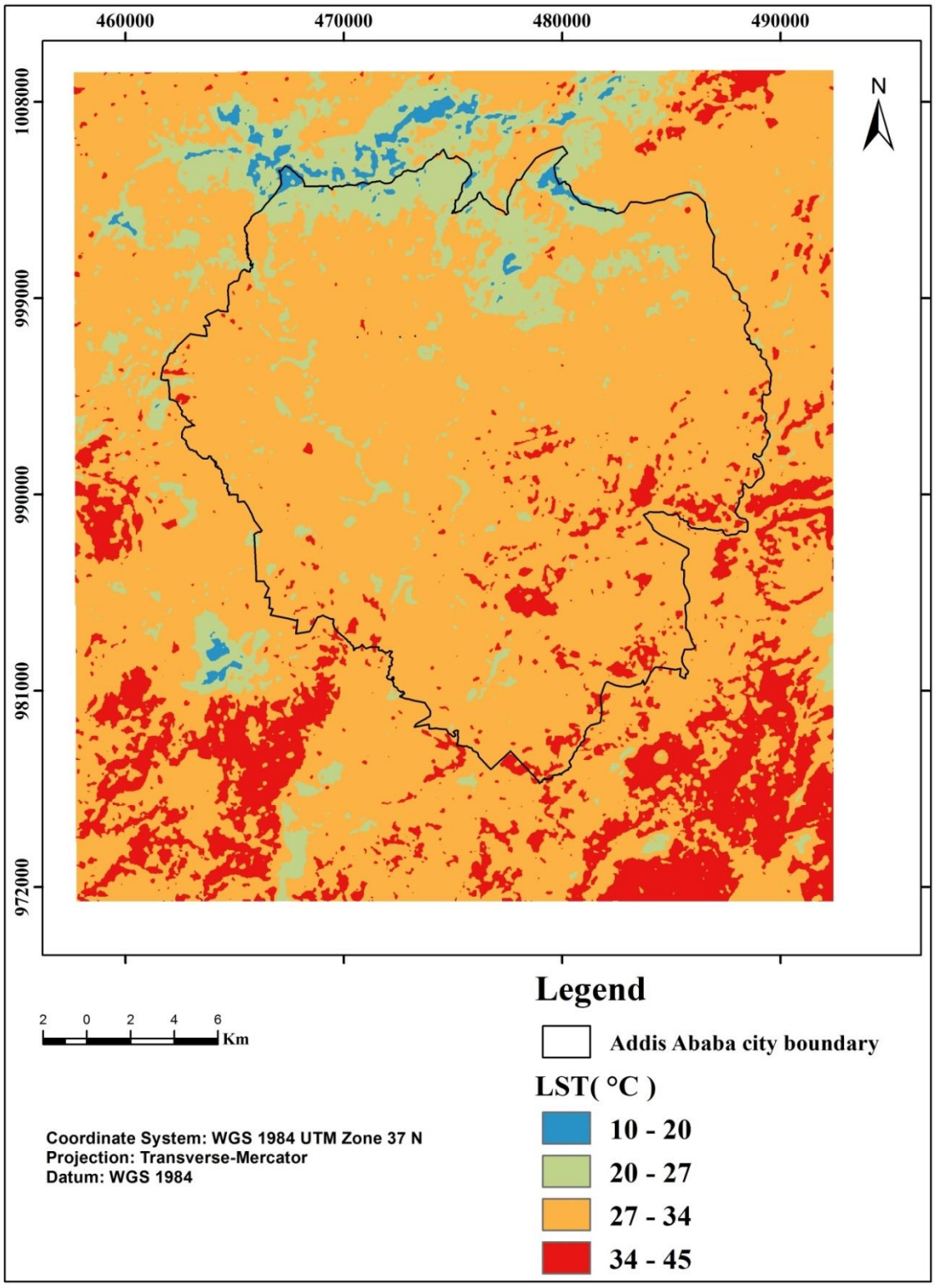

Figure 4.17: Predicted LST map of the study area for the year 2050

4.8.3 Comparison of Mean LST in each LULC class between 2020 and 2050

Figure 4.18 shows the comparison of mean LST in each LULC between 2020 and 2050. The mean LST in the water body and vegetation area was predicted to decrease by 0.70 ^{0}C and 1.05 ^{0}C, respectively from 2020 to 2050. But, the mean LST in agricultural land and the built-up area was predicted to increase by 0.22 ^{0}C and 0.10 ^{0}C, respectively between the same years in the study area.

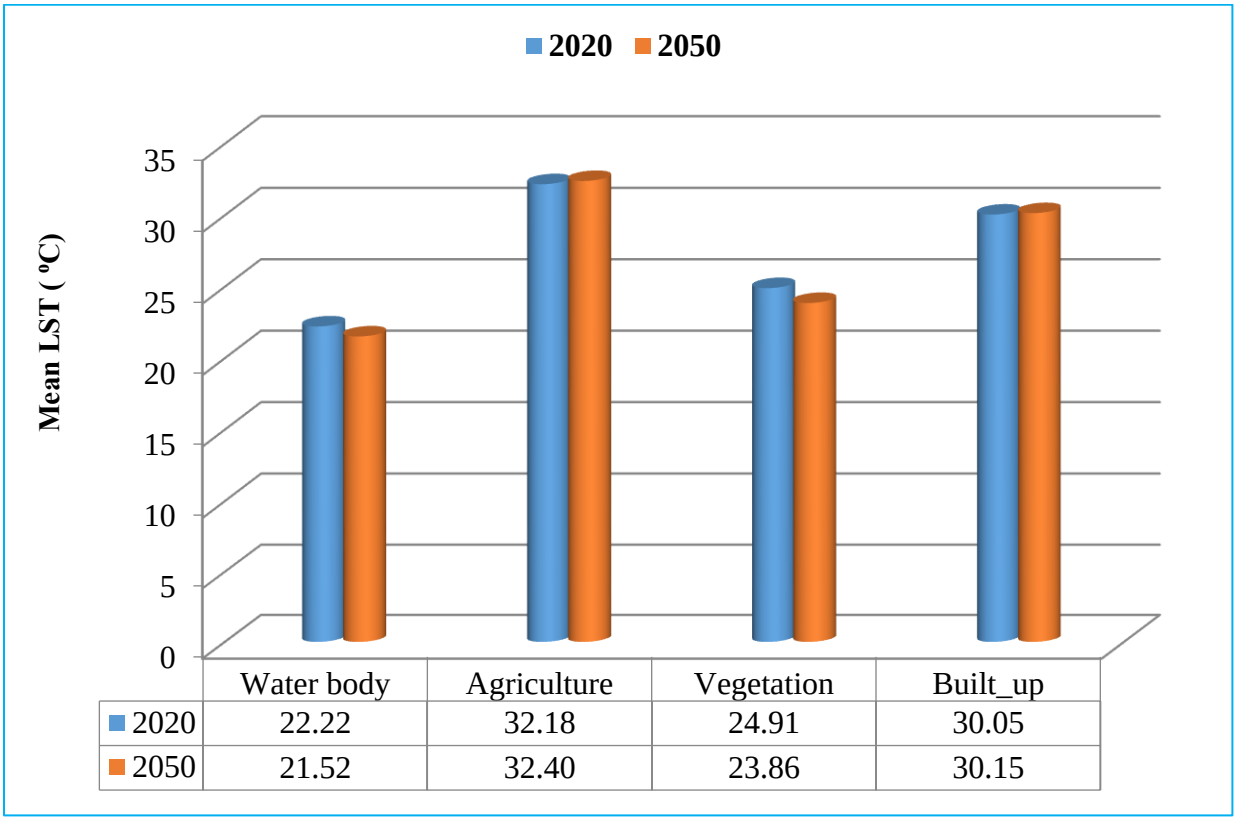

	Water body	Agriculture	Vegetation	Built_up
2020	22.22	32.18	24.91	30.05
2050	21.52	32.40	23.86	30.15

Figure 4.18: Comparison of mean LST in each LULC between 2020 and 2050

CHAPTER 5 DISCUSSIONS

An investigation on the dynamics of LULC across Addis Ababa and its surrounding by this study revealed the increased need for land for urban expansion. Accordingly, the built-up area coverage was increased from 8884.44 ha to 46884 ha from 1991 to 2020 and was predicted to cover 72897.5 ha by the year 2050 with the consideration of other LULC classes. This was supported by the other study in Ethiopia that focused on the requirement of land by the cities and towns in Ethiopia for urban expansion(Terfa et al., 2019). This was also supported by the study in Adama Zuria that stated the need for land for urban expansion(Tafesse and Suryabhagavan, 2019). A study by Lencho (2019), on the Spatio-temporal LULC changes of Burayu town between 1990 and 2019, predicted the extent that would have been by the year 2050. The result revealed that an increment of the built-up area from 100 ha in 1990 to 4100 ha in 2019 with an expected prediction of 5200 ha by the year 2050. Thus, this was also consistent with the findings of the current study.

The higher NDVI values corresponded to vegetation areas in the north and eastern part of the study area including mount Entoto. The lower NDVI values were observed in Lake Gefersa and Aba Samuel. The central parts of the study area including Addis Ababa city have medium NDVI values. Several studies showed that healthy green vegetation area has higher NDVI values(Chu et al., 2019, Johansen and Tømmervik, 2014). During the dry season, certain types of vegetation have higher reflectance to SWIR resulting in higher NDBI(Zhang et al., 2009a). Some studies showed the agricultural land has high NDBI values similar to the built-up area. This improves the performance of NDBI to predict LST that both agricultural land and built-up area have higher NDBI values(Pu et al., 2006).

The result from correlation analysis between several LCI and LST indicated that the NDBI was found as the best predictor of LST($R = 0.72$). During the selection of the best predictor, those highly correlated to each other than with LST were neglected and only the one highly correlated with LST was selected to minimize a multi-collinearity error. A similar study by Mushore (2018) selected only UI from several LCI to overcome the stated errors. But, another study selected three indices(NDBI, NDBsI, and MNDWI) for the prediction of LSTs in Saudi Arabia without stating the multi-collinearity error(Rahman et al., 2017). The relationship between NDBI and LST in different studies showed that there is a strong positive correlation between NDBI and

LST(Kawamura, 1996, Zhang et al., 2009b, Rahman et al., 2017). The performance of the regression model to predict LST indicated that LST for 2050 was predicted with high accuracy (MAPE = 9.4 %)(Lewis, 1982). As reported by Ahmed et al, (2013) a linear regression model was recommended for the prediction of the future LST.

The accuracy assessment between the classified map and the modeled map for 2020 indicated that the two maps were substantially agreed to each other with KIA = 0.70 and continued to predict future LULC change for 2050. A similar study by Lencho (2019) on Spatio-temporal modeling of LULC found a moderate agreement between the simulated and classified map of 2019 and continued to predict for the year 2050. Another study observed better similarity between the modeled and the classified map 2015 in Harare city and proceed to predict for 2025, 2035, and 2045(Mushore et al., 2018). From the predicted LULC change of 2050, the coverage of the built-up area was predicted to increase at the expense of water body vegetation and agricultural lands. The result is consistent with worldwide expectations that urban residents will rise causing an increase of built-up areas with the decrease of other LULC classes(Ahmed and Ahmed, 2012, Araya and Cabral, 2010).

The finding from the Spatio-temporal analysis of LST indicated that the highest mean LST (30.32 ^{0}c) was observed in 2020 and the lowest mean LST (22.92 ^{0}c) was observed in 1991. But, the mean LST observed in 2002 was higher than the mean LST observed in 2011. Additionally, the result indicated that the area coverage of the lower categories (10 – 20 ^{0}c, 20 – 27 ^{0}c, and 27 – 34 ^{0}c) was predicted to decrease while the area covered by the highest category (34 – 45) was predicted to increase in 2050. The area covered by the highest category was 0.00% in 1991 and 12.13% in 2020. This warmer category of LST was predicted to cover 14.66% in 2050. This result was consistent with several studies conducted on modeling future LST(Mushore et al., 2018, Rahman et al., 2017, Maduako et al., 2016). When compared to other LULC classes, the highest mean LST (32.18 ^{0}C) was observed in agricultural land in the year 2020. In the future prediction of 2050, the agricultural land was predicted to have a higher mean LST mostly in the southern part of the study area.

The predicted result revealed that the LST may rise in areas within the same LULC between 2020 and 2050. This was supported by other studies focused on climate change and concluded that global warming will affect areas that are not part of urban expansion(Argüeso et al., 2014, Dereczynski et al., 2013). On the other hand, the rise of LSTs patterns is in reaction to LULC modifications in which the coverage built-up areas may increase at the expense of green-spaces and wetlands(Mushore et al., 2018).

The northern parts of the study area had a higher coverage of vegetation areas and were found relatively cooler than southern and eastern areas. Even though the coverage of the built-up area increases in the central part of the study area, the availability of green vegetation in the city is higher than in the southern part of the study area. This abundance of vegetation makes the area to have a lower LST than the southern area. Additionally, the southern part of Addis Ababa city is characterized by agricultural land and has a lower elevation than other places in the study area. This may affect the distribution of LST throughout the study area. The highest LST category (34 - 45 ^{0}C) is expected to cover a larger area in the southern part of the study area in the future prediction of 2050 than the coverage in 2020 and before.

CHAPTER 6 CONCLUSIONS AND RECOMMENDATIONS

6.1 Conclusions

The study aimed at predicting the future LST distribution of Addis Ababa city and its surrounding area using CA-Markov analysis. The LULC maps were produced for the years 1991, 2002, 2011, and 2020 with high accuracy. Based on the classified map of the study area between 1991 and 2020; the coverage of built-up areas was increased rapidly while the coverage of water bodies, agricultural land, and vegetation areas was decreased in the past three decades. Similarly, a significant Spatio-temporal variation of LST was observed between 1991 and 2020 in the study area. From the results, it was concluded that the northern parts of the study area including mount Entoto have a relatively cooler temperature than the central and southern parts of the study area due to the higher coverage of vegetation. On the other hand, the southern parts of the study area have a warmer temperature. From the comparison of temporal mean LST between each LULC, it was concluded that the agricultural land has the highest mean LST than the others. But, the area has a lower elevation when compared to other the central and the northern part of the study area. Thus, the study recommended the future study to address the impact of topography on the distribution of LST.

Based on the evaluation of several LCIs to predict the future LST of Addis Ababa city and its surrounding areas, it can be concluded that NDBI can predict the future LST of 2050 better than other LCIs. The validation result of the CA-Markov model indicated that there was a substantial agreement between the classified LULC map and the modeled LULC map of 2020. From the predicted LULC map of Addis Ababa city and surroundings, it can be concluded that the coverage of the built-up area was predicted to increase while the coverage of waterbody, agricultural land, and vegetation land was predicted to decrease in the year 2050. Similarly, the area coverage of the warmer category of LST was predicted to increase while the lower categories of LST were predicted to decrease in the next 30 years. Generally, the current rising trend of LST will continue in the next three decades due to the dynamics of LULC and the variability of climate in the study area. To minimize this, proper environmental protection measures like planting trees should be taken. Hence, the application of CA-Markov analysis for the prediction of future LST from Remotely Sensed data is efficient and can address a larger area.

6.2 Recommendations

The study was focused on the prediction of future LST from Spato-temporal LULC dynamics in Addis Ababa city and its surrounding area. The study revealed that the mean LST of Addis Ababa city and its surrounding area was increased by 8 ^{0}C from 1991 to 2020 and was predicted to rise in 2050. From the study results, the following recommendations have been drawn.

- The finding of the study revealed that the rise of LST was observed from 1991 to 2020 and was predicted to increase in the study area for 2050. The future prediction may not look like the predicted LST if environmental protection measures will be applied. So, the study will help the environmentalist and city planners in their decision making by providing the rising trend of LST.
- Future studies should inspect the socioeconomic impact of the rise of predicted LST.
- The warmer temperature was observed in the southern part of the study area. Unfortunately, the area has a lower elevation when compared to the cooler part. Hence, the study recommended that the future study should account for the influences of elevation on the LST variation.
- Generally, the results of the study underline the significance of satellite data for the prediction of future LULC and LST using CA-Markov chain analysis. However, future studies should evaluate the viability of this method at regional scales. This will help to take early measures at regional scales before serious environmental problems arise.

REFERENCES

ABRAHA, H. 2012. *Impact of Land Use Land Cover Change on Land Surface.* Addis Ababa University.

ADHIKARI, S. & SOUTHWORTH, J. 2012. Simulating forest cover changes of Bannerghatta National Park based on a CA-Markov model: a remote sensing approach. *Remote Sensing,* 4**,** 3215-3243.

ADINNA, E., CHRISTIAN, E. I. & OKOLIE, A. T. 2009. Assessment of urban heat island and possible adaptations in Enugu urban using landsat-ETM. *Journal of Geography and Regional Planning,* 2**,** 030-036.

AGARWAL, C. 2002. *A review and assessment of land-use change models: dynamics of space, time, and human choice*, US Department of Agriculture, Forest Service, Northeastern Research Station.

AHMED, B. & AHMED, R. 2012. Modeling urban land cover growth dynamics using multi-temporal satellite images: a case study of Dhaka, Bangladesh. *ISPRS International Journal of Geo-Information,* 1**,** 3-31.

AHMED, B., KAMRUZZAMAN, M., ZHU, X., RAHMAN, M. & CHOI, K. 2013. Simulating land cover changes and their impacts on land surface temperature in Dhaka, Bangladesh. *Remote Sensing,* 5**,** 5969-5998.

AKBARI, H., POMERANTZ, M. & TAHA, H. 2001. Cool surfaces and shade trees to reduce energy use and improve air quality in urban areas. *Solar energy,* 70**,** 295-310.

ALHAWITI, R. H. & MITSOVA, D. 2016. Using landsat-8 data to explore the correlation between urban heat island and urban land uses. *IJRET: International Journal of Research in Engineering and Technology,* 5**,** 457-466.

ALI, H. 2009. *Land use and land cover change, drivers and its impact: A comparative study from Kuhar Michael and Lenche Dima of Blue Nile and Awash Basins of Ethiopia.* Cornell University.

AMIRI, R., WENG, Q., ALIMOHAMMADI, A. & ALAVIPANAH, S. K. 2009. Spatial–temporal dynamics of land surface temperature in relation to fractional vegetation cover and land use/cover in the Tabriz urban area, Iran. *Remote sensing of environment,* 113**,** 2606-2617.

ARAYA, Y. H. & CABRAL, P. 2010. Analysis and modeling of urban land cover change in Setúbal and Sesimbra, Portugal. *Remote Sensing,* 2**,** 1549-1563.

ARGÜESO, D., EVANS, J. P., FITA, L. & BORMANN, K. J. 2014. Temperature response to future urbanization and climate change. *Climate Dynamics,* 42**,** 2183-2199.

ARSANJANI, J. J., HELBICH, M., KAINZ, W., BOLOORANI, A. D. J. I. J. O. A. E. O. & GEOINFORMATION 2013. Integration of logistic regression, Markov chain and cellular automata models to simulate urban expansion. 21**,** 265-275.

BALEW, A. 2018. *Impacts of Land-Use and Land-Cover Changes on Land Surface Temperature Distribution In Bahir Dar Town and Its Surroundings Using Remote Sensing.* Addis Ababa University.

BALOLOY, A. B., BLANCO, A. C., CANDIDO, C. G., ARGAMOSA, R. J. L., DUMALAG, J. B. L. C., DIMAPILIS, L. L. C. & PARINGIT, E. C. 2018. Estimation of mangrove forest aboveground biomass using multispectral bands, vegetation indices and biophysical variables derived from optical satellite imageries: rapideye, planetscope and sentinel-2. *ISPRS Annals of Photogrammetry, Remote Sensing & Spatial Information Sciences,* 4.

BANTIDER, A., HURNI, H. & ZELEKE, G. 2011. Responses of rural households to the impacts of population and land-use changes along the Eastern Escarpment of Wello, Ethiopia. *Norsk Geografisk Tidsskrift-Norwegian Journal of Geography,* 65**,** 42-53.

BEHERA, M., BORATE, S. N., PANDA, S. N., BEHERA, P. R. & ROY, P. S. 2012. Modelling and analyzing the watershed dynamics using Cellular Automata (CA)–Markov model–A geo-information based approach. *Journal of earth system science,* 121**,** 1011-1024.

BENAYAS, J. R., MARTINS, A., NICOLAU, J. M. & SCHULZ, J. J. 2007. Abandonment of agricultural land: an overview of drivers and consequences. *CAB reviews: Perspectives in agriculture, veterinary science, nutrition and natural resources,* 2**,** 1-14.

BURGAN, F. & HARTFORD, F. 1993. Monitoring vegetation greenness with satellite data. Ogden, UT: USDA, Forest Service, Intermountain Forest and Range Experiment Station. *General Technical Report INT,* 297.

CHANDER, G., MARKHAM, B. L. & HELDER, D. L. 2009. Summary of current radiometric calibration coefficients for Landsat MSS, TM, ETM+, and EO-1 ALI sensors. *Remote sensing of environment,* 113**,** 893-903.

CHU, H., VENEVSKY, S., WU, C. & WANG, M. 2019. NDVI-based vegetation dynamics and its response to climate changes at Amur-Heilongjiang River Basin from 1982 to 2015. *Science of the Total Environment,* 650**,** 2051-2062.

COLWELL, J. E. 1974. Vegetation canopy reflectance. *Remote sensing of environment,* 3**,** 175-183.

CONGALTON, R. G. J. R. S. O. G. C. F. F. S. 2009. Accuracy and error analysis of global and local maps: Lessons learned and future considerations. 441.

CSA 2015. *Central Statistical Agency of Ethiopia, Annual Report: national-statistics-abstract/141-population*, Federal Democratic Republic of Ethiopia, Population Census Commission.

DERECZYNSKI, C., SILVA, W. L. & MARENGO, J. 2013. Detection and projections of climate change in Rio de Janeiro, Brazil.

DERIBEW, K. T. & DALACHO, D. W. 2019. Land use and forest cover dynamics in the North-eastern Addis Ababa, central highlands of Ethiopia. *Environmental Systems Research,* 8**,** 8.

DESA, U. 2018. Revision of world urbanization prospects. *Population Division of the UN Department of Economic and Social Affairs, UN, New York. URL: https://population. un. org/wup*.

DI GREGORIO, A. 2005. *Land cover classification system: classification concepts and user manual: LCCS*, Food & Agriculture Org.

EASTMAN, J. 2012a. IDRISI Selva manual. *Clark University, Worcester*, 324.

EASTMAN, J., VAN FOSSEN, M., SOLARZANO, L. J. G., SPATIAL ANALYSIS & MODELING 2005. Transition potential modeling for land cover change. 357-386.

EASTMAN, J. J. I. P., CLARK LABS-CLARK UNIVERSITY 2012b. Idrisi selva tutorial. 45, 51-63.

EASTMAN, J. R. 2006. IDRISI Andes tutorial. *Clark Labs., Clark University, Worcester, MA*.

EL-NAHRY, A. & RASHASH, A. Impact of industrial areas on surface temperature using thermal infrared remote sensing and GIS techniques a case study of Jubail City, KSA. Dammam, Eastern Province, Saudi Arabia: The Eight National GIS Symposium in Saudi Arabia, 2013.

ELLIS, E. & PONTIUS JR, R. J. E. P. 2006. Land-use and land-cover change—encyclopedia of earth. 2, 142-153.

FAN, M. & SHIBATA, H. 2015. Simulation of watershed hydrology and stream water quality under land use and climate change scenarios in Teshio River watershed, northern Japan. *Ecological Indicators,* 50, 79-89.

FAO 2002. Africover.

FAO, U. 1999. Terminology for integrated resources planning and management. *Food and Agriculture Organization/United Nations Environmental Programme, Rome, Italy/Nairobi, Kenia*.

FOODY, G. M. 2002. Status of land cover classification accuracy assessment. *Remote sensing of environment,* 80, 185-201.

GEZIE, M. 2019. Farmer's response to climate change and variability in Ethiopia: A review. *Cogent Food & Agriculture,* 5, 1613770.

GIL, J. 2005. Modelling TCP with a Discrete Time Markov Chain. *HET-NETs: Performance Modelling and Evaluation of Heterogenous Networks*.

GLUCH, R., QUATTROCHI, D. A. & LUVALL, J. C. J. R. S. O. E. 2006. A multi-scale approach to urban thermal analysis. 104, 123-132.

HOFFMANN, P., KRUEGER, O. & SCHLÜNZEN, K. H. J. I. J. O. C. 2012. A statistical model for the urban heat island and its application to a climate change scenario. 32, 1238-1248.

HOUGHTON, R. A. 1994. The worldwide extent of land-use change. *BioScience,* 44, 305-313.

HU, Y. & JIA, G. 2010. Influence of land use change on urban heat island derivedfrom multi-sensor data. *International Journal of Climatology,* 30, 1382-1395.

HU, Z., LO, C. J. C., ENVIRONMENT & SYSTEMS, U. 2007. Modeling urban growth in Atlanta using logistic regression. 31, 667-688.

HUETE, A. 1988. Huete, AR A soil-adjusted vegetation index (SAVI). Remote Sensing of Environment. *Remote sensing of environment,* 25, 295-309.

JENSEN, J. R. 1996. *Introductory digital image processing: a remote sensing perspective*, Prentice-Hall Inc.

JIANG, J. & TIAN, G. J. P. E. S. 2010. Analysis of the impact of land use/land cover change on land surface temperature with remote sensing. 2**,** 571-575.

JIMÉNEZ-MUÑOZ, J. C., SOBRINO, J. A., PLAZA, A., GUANTER, L., MORENO, J. & MARTÍNEZ, P. 2009. Comparison Between Fractional Vegetation Cover Retrievals from Vegetation Indices and Spectral Mixture Analysis: Case Study of PROBA/CHRIS Data Over an Agricultural Area. *Sensors (Basel, Switzerland),* 9**,** 768-793.

JOHANSEN, B. & TØMMERVIK, H. 2014. The relationship between phytomass, NDVI and vegetation communities on Svalbard. *International Journal of Applied Earth Observation and Geoinformation,* 27**,** 20-30.

JULIEN, Y. & SOBRINO, J. A. 2009. The Yearly Land Cover Dynamics (YLCD) method: An analysis of global vegetation from NDVI and LST parameters. *Remote sensing of environment,* 113**,** 329-334.

KAWAMURA, M. Relation between social and environmental conditions in Colombo Sri Lanka and the urban index estimated by satellite remote sensing data. Proc. 51st Annual Conference of the Japan Society of Civil Engineers, 1996. 190-191.

KAYET, N., PATHAK, K., CHAKRABARTY, A., SAHOO, S. J. M. E. S. & ENVIRONMENT 2016. Spatial impact of land use/land cover change on surface temperature distribution in Saranda Forest, Jharkhand. 2**,** 127.

KESHTKAR, H., VOIGT, W. J. M. E. S. & ENVIRONMENT 2016. A spatiotemporal analysis of landscape change using an integrated Markov chain and cellular automata models. 2**,** 10.

KOCH, G. G., LANDIS, J. R., FREEMAN, J. L., FREEMAN JR, D. H. & LEHNEN, R. G. 1977. A general methodology for the analysis of experiments with repeated measurement of categorical data. *Biometrics***,** 133-158.

KOTTEK, M., GRIESER, J., BECK, C., RUDOLF, B. & RUBEL, F. J. M. Z. 2006. World map of the Köppen-Geiger climate classification updated. 15**,** 259-263.

LEMLEM, A. 2007. *Assessing the impact of land use and land cover change on groundwater recharge using Rs and Gis; a case of Awassa catchement, Southern Ethiopia.* M. Sc. Thesis. Addis Ababa University, Ethiopia.

LEWIS, C. D. 1982. *Industrial and business forecasting methods: A practical guide to exponential smoothing and curve fitting*, Butterworth-Heinemann.

LI, F. 2012. Investigation of urban sprawl on the basis of remote sensing data: a case study in Jiangning, Nanjing City, China.

LO, C., QUATTROCHI, D. A. J. P. E. & SENSING, R. 2003. Land-use and land-cover change, urban heat island phenomenon, and health implications. 69**,** 1053-1063.

MACLEAN, M. G. & CONGALTON, R. G. Map accuracy assessment issues when using an object-oriented approach. Proceedings of the American Society for Photogrammetry and Remote Sensing 2012 Annual Conference, Sacramento, CA, USA, 2012. 19-23.

MADUAKO, I., YUN, Z. & PATRICK, B. 2016. Simulation and prediction of land surface temperature (LST) dynamics within Ikom City in Nigeria using artificial neural network (ANN). *Journal of Remote Sensing & GIS,* 5**,** 1-7.

MARKHAM, B. & BARKER, J. 1986. Landsat MSS and TM post-calibration dynamic ranges, exoatmospheric reflectances and at-satellite temperatures, EOSAT Landsat Technical Notes No. 1. *Lanham, Md*.

MEYER, W. B. & TURNER, B. L. 1992. Human population growth and global land-use/cover change. *Annual review of ecology and systematics,* 23**,** 39-61.

MIHERETU, B. A. & YIMER, A. A. 2018. Land use/land cover changes and their environmental implications in the Gelana sub-watershed of Northern highlands of Ethiopia. *Environmental Systems Research,* 6**,** 7.

MOGHADAM, H. S. & HELBICH, M. 2013. Spatiotemporal urbanization processes in the megacity of Mumbai, India: A Markov chains-cellular automata urban growth model. *Applied Geography,* 40**,** 140-149.

MOHAMED, A. & WORKU, H. 2019. Simulating urban land use and cover dynamics using cellular automata and Markov chain approach in Addis Ababa and the surrounding. *Urban Climate,* 31**,** 1-17.

MUSHORE, T. D., MUTANGA, O., ODINDI, J. & DUBE, T. 2018. Determining extreme heat vulnerability of Harare Metropolitan City using multispectral remote sensing and socio-economic data. *Journal of Spatial Science,* 63**,** 173-191.

NMA 2007. Climate change national adaptation program of action (NAPA) of Ethiopia. The Federal Democratic Republic of Ethiopia, Ministry of Water Resources ….

ODINDI, J., BANGAMWABO, V. & MUTANGA, O. J. I. J. O. E. R. 2015. Assessing theValue ofUrbanGreen Spaces inMitigatingMulti-SeasonalUrban Heat usingMODISLand SurfaceTemperature (LST) andLandsat 8 data. 9**,** 9-18.

OMAR, N. & SANUSI, S. Markov-CA model using analytical hierarchy process and multiregression technique. IOP conference series: earth and environmental science, 2014. IOP Publishing, 012008.

OMRAN, E.-S. E. 2012. Detection of land-use and surface temperature change at different resolutions.

OYLER, J. W. 2016. Remotely sensed land skin temperature as a spatial predictor of air temperature across the conterminous United States. *Journal of Applied Meteorology and Climatology,* 55**,** 1441-1457.

PARRY, M., PARRY, M. L., CANZIANI, O., PALUTIKOF, J., VAN DER LINDEN, P. & HANSON, C. 2007. *Climate change 2007-impacts, adaptation and vulnerability: Working group II contribution to the fourth assessment report of the IPCC,* Cambridge University Press.

PERUMAL, K. & BHASKARAN, R. 2010. Supervised classification performance of multispectral images. *arXiv preprint arXiv:1002.4046*.

PONTIUS, G. R. & MALANSON, J. 2005. Comparison of the structure and accuracy of two land change models. *International Journal of Geographical Information Science,* 19**,** 243-265.

PONTIUS JR, R. G. & CHEN, H. 2006. GEOMOD modeling. *Clark University*.

PU, R., GONG, P., MICHISHITA, R. & SASAGAWA, T. 2006. Assessment of multi-resolution and multi-sensor data for urban surface temperature retrieval. *Remote Sensing of Environment,* 104**,** 211-225.

QIANG, Y. & LAM, N. S. 2015. Modeling land use and land cover changes in a vulnerable coastal region using artificial neural networks and cellular automata. *Environmental monitoring and assessment,* 187**,** 57.

QIN, D., PLATTNER, G., TIGNOR, M., ALLEN, S., BOSCHUNG, J., NAUELS, A., XIA, Y., BEX, V. & MIDGLEY, P. 2014. Climate change 2013: the physical science basis. *Contribution of Working Group I to the Fifth Assessment Report of the Intergovernmental Panel on Climate Change (eds TF Stocker et al.)***,** 5-14.

RAHAMAN, K. R., AHMED, M. R. & HASSAN, Q. K. J. I. I. J. O. G.-I. 2018. Using satellite-borne remote sensing data in generating local warming maps with enhanced resolution. 7**,** 398.

RAHMAN, M. T., ALDOSARY, A. S. & MORTOJA, M. 2017. Modeling future land cover changes and their effects on the land surface temperatures in the Saudi Arabian eastern coastal city of Dammam. *Land,* 6**,** 36.

RAJESHWARI, A. & MANI, N. 2014. Estimation of land surface temperature of Dindigul district using Landsat 8 data. *International Journal of Research in Engineering and Technology,* 3**,** 122-126.

RAMACHANDRA, T., BHARATH, H. J. I. J. O. E. T. & ENGINEERING, A. 2012. Spatio-Temporal Pattern of Landscape Dynamics in Shimoga, Tier II City, Karnataka State, India. 2**,** 563-576.

RAO, P. K. J. B. O. T. A. M. S. 1972. Remote sensing of urban" heat islands" from an environmental satellite. 53**,** 647-648.

REGMI, R., SAHA, S. & SUBEDI, D. 2017. Geospatial analysis of land use land cover change modeling in Phewa Lake watershed of Nepal by using GEOMOD model. *Himalayan Physics***,** 65-72.

SANTANA, L. M. J. I. J. O. R. S. 2007. Landsat ETM+ image applications to extract information for environmental planning in a Colombian city. 28**,** 4225-4242.

SCHIFF, J. L. 2011. *Cellular automata: a discrete view of the world,* John Wiley & Sons.

SMITH, K. R., ROEBBER, P. J. J. J. O. A. M. & CLIMATOLOGY 2011. Green roof mitigation potential for a proxy future climate scenario in Chicago, Illinois. 50**,** 507-522.

SOBRINO, J., RAISSOUNI, N. & LI, Z.-L. 2001. A comparative study of land surface emissivity retrieval from NOAA data. *Remote Sensing of Environment,* 75**,** 256-266.

SOBRINO, J. A., JIMÉNEZ-MUÑOZ, J. C. & PAOLINI, L. 2004. Land surface temperature retrieval from LANDSAT TM 5. *Remote Sensing of environment,* 90**,** 434-440.

STORY, M. & CONGALTON, R. G. 1986. Accuracy assessment: a user's perspective. *Photogrammetric Engineering and remote sensing,* 52**,** 397-399.

SUNG, C. Y. J. U. F. & GREENING, U. 2013. Mitigating surface urban heat island by a tree protection policy: A case study of The Woodland, Texas, USA. 12**,** 474-480.

TAFESSE, B. 2017. *Impact of land-use/land-cover changes on land surface temperature in Adama Zuria Woreda, Ethiopia, using geospatial tools.* Addis Ababa Universty.

TAFESSE, B. & SURYABHAGAVAN, K. 2019. Systematic modeling of impacts of land-use and land-cover changes on land surface temperature in Adama Zuria District, Ethiopia. *Modeling Earth Systems and Environment,* 5**,** 805-817.

TEFERA, B. 2002. *Nature and causes of land degradation in the Oromiya Region: A review*, ILRI (aka ILCA and ILRAD).

TERFA, B. K., CHEN, N., LIU, D., ZHANG, X. & NIYOGI, D. 2019. Urban expansion in Ethiopia from 1987 to 2017: Characteristics, spatial patterns, and driving forces. *Sustainability,* 11**,** 2973.

TRAN, H., UCHIHAMA, D., OCHI, S., YASUOKA, Y. J. I. J. O. A. E. O. & GEOINFORMATION 2006. Assessment with satellite data of the urban heat island effects in Asian mega cities. 8**,** 34-48.

TUCKER, C. J. 1979. Red and photographic infrared linear combinations for monitoring vegetation. *Remote sensing of Environment,* 8**,** 127-150.

TURVEY, C. G. & MCLAURIN, M. K. 2012. Applicability of the normalized difference vegetation index (NDVI) in index-based crop insurance design. *Weather, Climate, and Society,* 4**,** 271-284.

USEPA 2004. *Guidelines for water reuse*, US Environmental Protection Agency.

USGS 2016. Landsat 8 (L8) data users handbook. *Department of the Interior US Geological Survey, LSDS-1574*.

VAN DE GRIEND, A. & OWE, M. 1993. On the relationship between thermal emissivity and the normalized difference vegetation index for natural surfaces. *International Journal of remote sensing,* 14**,** 1119-1131.

WENG, Q. & LARSON, R. C. 2005. Satellite remote sensing of urban heat islands: current practice and prospects. *Geo-spatial technologies in urban environments.* Springer.

WENG, Q., LU, D. & SCHUBRING, J. 2004. Estimation of land surface temperature–vegetation abundance relationship for urban heat island studies. *Remote sensing of Environment,* 89**,** 467-483.

WENG, Q. J. J. O. E. M. 2002. Land use change analysis in the Zhujiang Delta of China using satellite remote sensing, GIS and stochastic modelling. 64**,** 273-284.

WOLFRAM, S. 1983. Statistical mechanics of cellular automata. *Reviews of modern physics,* 55**,** 601.

XIONG, Y., HUANG, S., CHEN, F., YE, H., WANG, C. & ZHU, C. 2012. The impacts of rapid urbanization on the thermal environment: A remote sensing study of Guangzhou, South China. *Remote sensing,* 4**,** 2033-2056.

XU, L., XIE, X. & LI, S. J. E. P. 2013. Correlation analysis of the urban heat island effect and the spatial and temporal distribution of atmospheric particulates using TM images in Beijing. 178**,** 102-114.

YE, H., WANG, K., HUANG, S., CHEN, F., XIONG, Y. & ZHAO, X. 2010. Urbanisation effects on summer habitat comfort: A case study of three coastal cities in southeast China. *International Journal of Sustainable Development & World Ecology,* 17**,** 317-323.

YUAN, F. & BAUER, M. E. J. R. S. O. E. 2007. Comparison of impervious surface area and normalized difference vegetation index as indicators of surface urban heat island effects in Landsat imagery. 106**,** 375-386.

YUE, W., XU, J., TAN, W. & XU, L. J. I. J. O. R. S. 2007. The relationship between land surface temperature and NDVI with remote sensing: application to Shanghai Landsat 7 ETM+ data. 28**,** 3205-3226.

ZELEKE, G. & HURNI, H. 2001. Implications of land use and land cover dynamics for mountain resource degradation in the Northwestern Ethiopian highlands. *Mountain research and development,* 21**,** 184-191.

ZHA, Y., GAO, J. & NI, S. 2003. Use of normalized difference built-up index in automatically mapping urban areas from TM imagery. *International journal of remote sensing,* 24**,** 583-594.

ZHANG, H., LI, Y. & GAO, X. 2009a. Potential impacts of land-use on climate variability and extremes. *Advances in Atmospheric Sciences,* 26**,** 840-854.

ZHANG, Y., ODEH, I. O. & HAN, C. 2009b. Bi-temporal characterization of land surface temperature in relation to impervious surface area, NDVI and NDBI, using a sub-pixel image analysis. *International Journal of Applied Earth Observation and Geoinformation,* 11**,** 256-264.

APPENDICES

Appendix 1: Change analysis (net change and gains and losses)

NET CHANGE (1991 – 2002, 2002 – 2011, 2011 – 2020, &1991 - 2020)

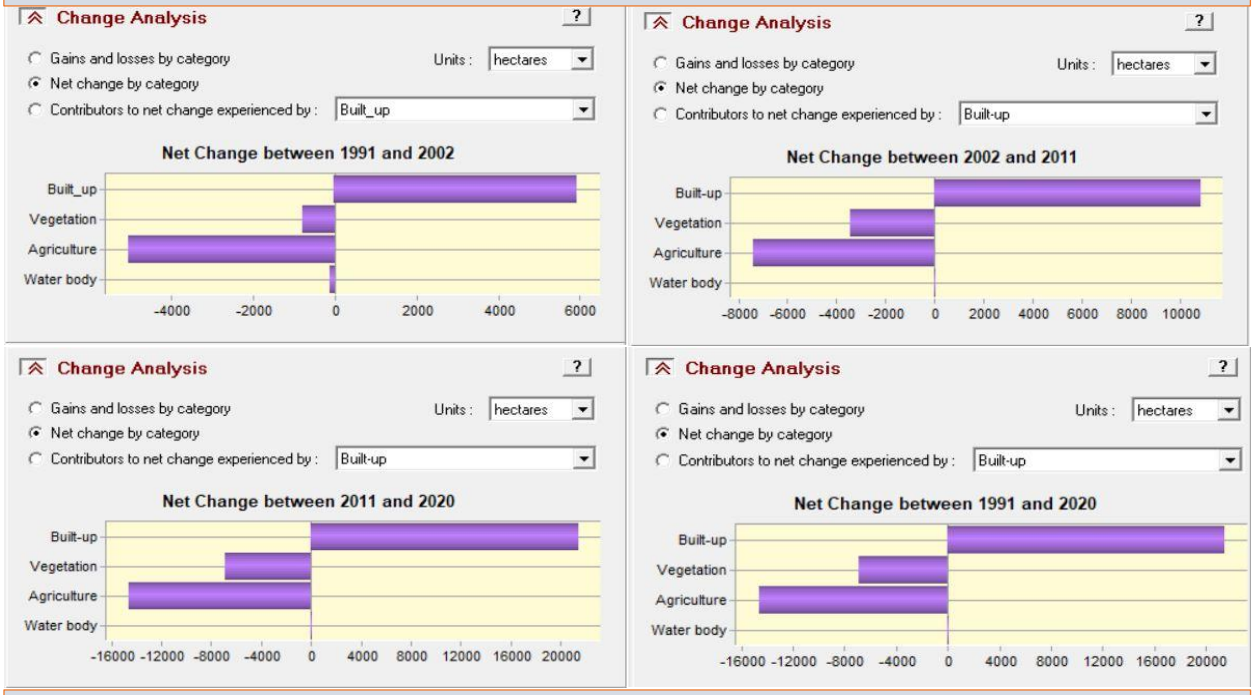

GAINS AND LOSSES (1991 – 2002, 2002 – 2011, 2011 – 2020, & 1991 - 2020)

Appendix 2: Markovian conditional probability map of predicted LULC 2020

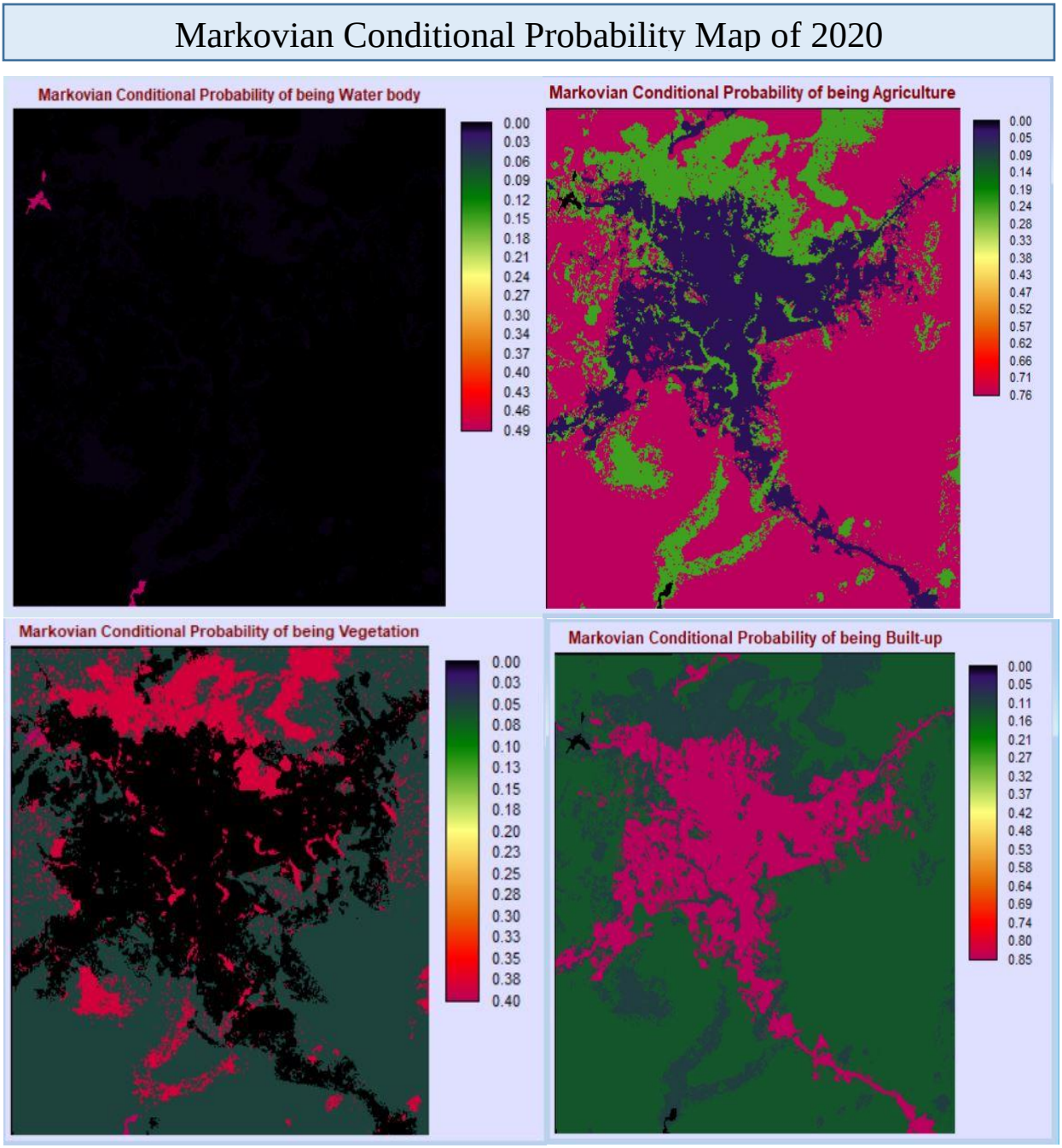

Appendix 3: Markovian conditional probability map of predicted LULC 2050

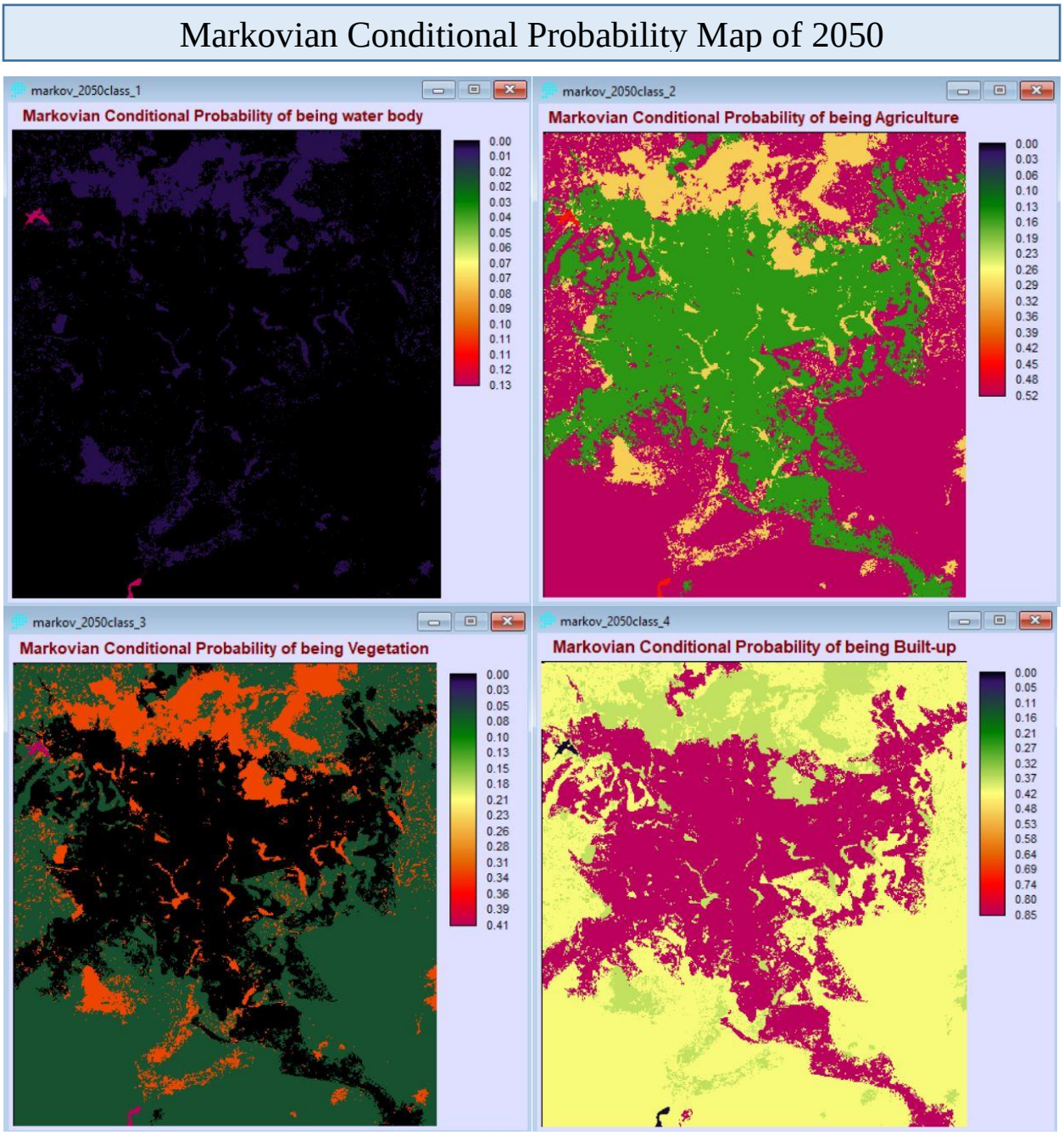

Appendix 4: classified NDBI map of 1991and 2020

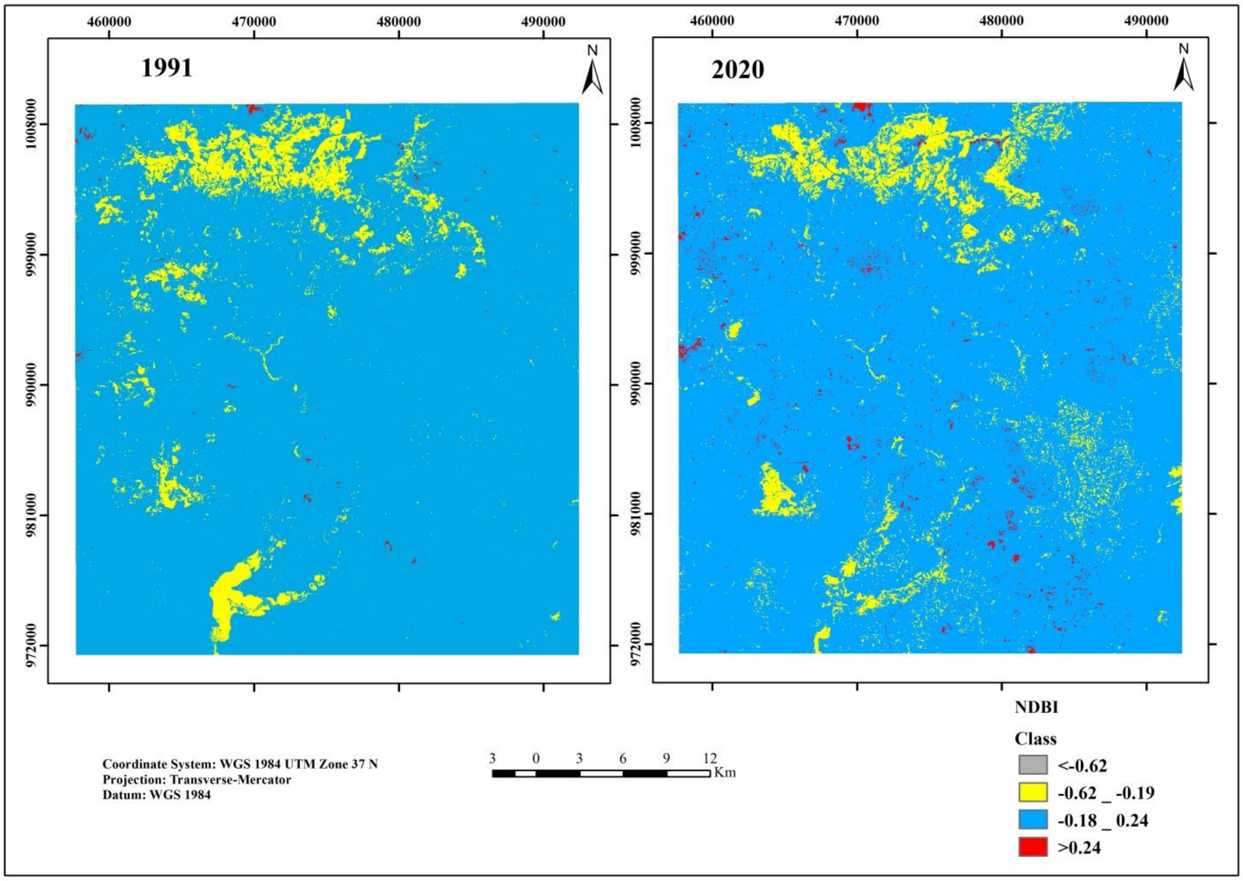

$$LST = 16.34 * NDBI + 30.07 \ldots \ldots (20)$$

The LST values were classified into four classes. Using the equation, the NDBI values were classified into four classes [10 – 20, 20 – 27, 27 – 34, and 34 – 45]

Then, NDBI maps were reclassified into the same class number so that they could predict each LST class. Each NDBI value corresponding to the LST value was calculated using equation (20)

For the example to get the upper limit of class 1 (NDBI corresponds to 20 ^{0}C) using the relationship:

NDBI = (LST – 30.07)/16.34, by rearranging the equation (20)

= (20 – 30.07)/16.34

= -10.07/16.34

= <u>-0.62</u> which corresponds to the 20^{0}C LST value

Appendix 5: predicted NDBI map of 2050